

An image-computable spatio-chromatic receptive  
field model of the midget retinal ganglion mosaic  
across the retina

Nicolas P. Cottaris<sup>1\*</sup>, Brian A. Wandell<sup>2</sup> and David H. Brainard<sup>1</sup>

<sup>1</sup>Department of Psychology, University of Pennsylvania, Philadelphia,  
PA, USA.

<sup>2</sup>Department of Psychology, Stanford University, Stanford, CA, USA.

\*Corresponding author(s). E-mail(s): [cottaris@upenn.edu](mailto:cottaris@upenn.edu);  
Contributing authors: [wandell@stanford.edu](mailto:wandell@stanford.edu); [brainard@upenn.edu](mailto:brainard@upenn.edu);

**Abstract**

Image-computable models of primate retinal ganglion cell (RGC) mosaics that are synthesized and constrained jointly by optical, anatomical and physiological properties, and which operate on images defined by their spatial-spectral radiance, do not currently exist. Here, we deploy a novel computational framework which synthesizes mosaics of linear spatio-chromatic receptive fields (RFs) of ON midget RGCs (mRGCs) by integrating published anatomical, physiological, and optical quality measurements, all varying with eccentricity. We use the synthesized mRGC mosaics to simulate both *in vivo* and *in vitro* physiological experiments and demonstrate the model's consistency with published data. The model enables computation of how visual performance is shaped by the representation of visual information provided by the linear spatiochromatic processing stage of midget RGCs. The developed computational framework carefully accounts for the effect of physiological optics on mRGC responses, enables comparison of *in vivo* and *in vitro* data, and allows exploration of how different assumptions about RF organization, such as selectivity for the type of cones pooled by the RF center mechanism, affect physiological responses and psychophysical performance. The open-source and freely available implementation provides a platform for understanding how the linear spatiochromatic receptive field representation of the mRGCs shapes visual performance, as well as a foundation for future work that incorporates response nonlinearities, temporal filtering, and extends to additional RGC mosaics.

**Keywords:** retinal ganglion cells, receptive field, model

047 **1 Introduction**

048

049 An important aim in computational visual neuroscience is to create accurate computer  
050 simulations of how neurons in the visual pathways encode and respond to visual scenes.  
051 These simulations, often called digital twins, are a quantitative description of the  
052 visual system. They enable links between the neural representation and perception  
053 and provide a tool for evaluating the effects of blinding disease and its treatment.

054 Over the last ten years we have built an open-source software platform, ISETBio  
055 (Image Systems Engineering Tools for Biology) [1], which serves as a digital twin for  
056 the initial stages of the human visual system. Previously, we described how ISETBio  
057 models (a) the formation of the retinal image, (b) the excitation of the cone pho-  
058 toreceptors, (c) phototransduction, and (d) fixational eye movements [2–4]. We and  
059 others have employed ISETBio to model human vision, including sensitivity to spa-  
060 tial contrast [2, 3], the impact of chromatic aberration on acuity [5], the encoding of  
061 information from natural images captured by cones [6], the effects of optics and cone  
062 density across the visual field on performance [7], and the influence of initial visual sig-  
063 nals on tasks like judging surface properties and lighting [8, 9]. We also used ISETBio  
064 to help interpret experimental measurements of retinal ganglion cells [10].

065 Here, we describe an extension of ISETBio which models the mosaic of a class of  
066 retinal ganglion cells (RGCs), the midget RGC (mRGC) mosaic. RGCs are the only  
067 pathway for information transmission from the retina to the brain, and their properties  
068 surely impact visual performance on many tasks. The spike trains transmitted via the  
069 axons of one million RGCs that form the human optic nerve, represent the signals  
070 from roughly 6.5 million cones and 110 million rods [11, 12]. Of these RGCs, mRGCs  
071 are a particularly important subtype, comprising 80% of the perifoveal RGCs and  
072 45% of the peripheral RGCs. In the very central fovea, it has been estimated that the  
073 mRGCs are 95% of the RGC population [13].

074 The role of the mRGCs in limiting spatial and color vision is still debated [14].  
075 Simulation of performance using image computable models of the mRGC mosaic offers  
076 a powerful tool for understanding the visual information encoded by these cells, espe-  
077 cially because they are very hard to measure and isolate experimentally. We have four  
078 primary goals for this human retina model.

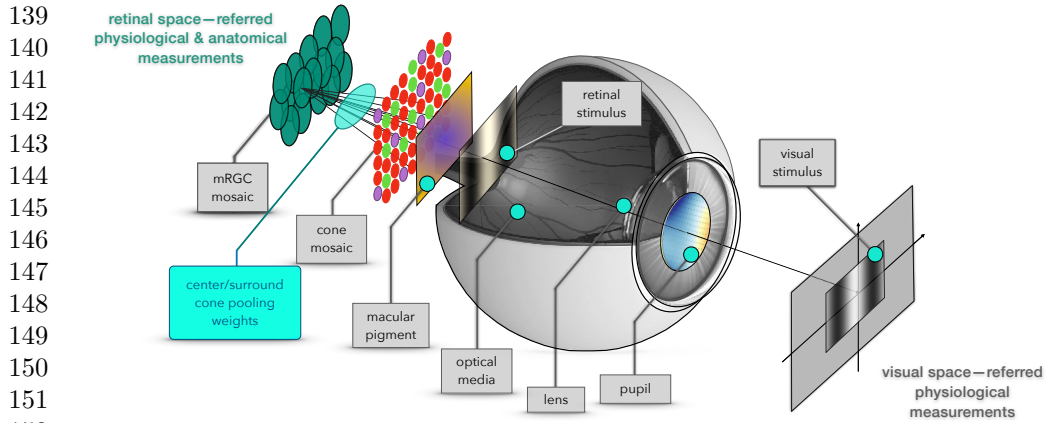
079 First, the model must distinguish the contributions of the eye’s optics and pho-  
080 toreceptors from the subsequent post-receptoral retinal circuitry. This separation is  
081 crucial for incorporating key physiological measurements, some of which are made *in*  
082 *vitro* without the eye’s optics. Failing to isolate the optical effects would prevent us  
083 from using this vital collection of data.

084 Second, the model must capture responses across a large portion of central  
085 retina. This is important because we and others are interested in how the retinal  
086 representation shapes performance not just in the fovea but also for peripheral viewing.

087 Third, the model must integrate diverse data types, including optical, anatomical,  
088 and physiological measurements. A comprehensive formulation is necessary because  
089 retinal ganglion cell (RGC) responses are shaped by all three of these factors.

090 Fourth, we aim for an extensible framework. The current implementation uses a  
091 linear spatiochromatic receptive field, which serves as a good initial approximation.  
092

The framework is designed to incorporate future extensions—such as response non-linearities, temporal dynamics, and additional RGC classes—to improve the model’s accuracy over time. The following points describe how our implementation achieves these goals.	093
1. <i>Separating representations.</i> Our mRGC model operates on the cone mosaic signals. This design isolates the post-receptoral circuitry (cone-to-mRGC), which is the pathway measured in <i>in vitro</i> experiments where the eye’s optics are removed [15, 16]. This separation is also valuable for interpreting experiments that use adaptive optics to eliminate optical blur [10]. While the components are separable, our implementation integrates the optics, cone sampling, and mRGC circuitry into a complete, image-computable pipeline. This full pathway allows us to simulate the transformation of a visual stimulus into an mRGC response, matching the conditions of <i>in vivo</i> measurements [17–19] and enabling predictions of human performance under natural viewing conditions.	094
2. <i>Representation across the visual field.</i> Visual performance varies across the visual field, and a key contribution of our model is that it allows computation of the mRGC representation continuously across the retina from the fovea out to 30°, along any meridian. Achieving this goal required implementation of novel algorithms for synthesizing mRGC RF mosaics.	095
3. <i>Multiple data types.</i> By explicitly representing different biological stages, our model enables algorithms that combine anatomical, physiological, and optical data. Incorporation of multiple types of measurements from the literature is critical because at present no one type of data sufficiently constrains mRGC properties across the visual field.	096
4. <i>Extensible.</i> The current implementation is a linear spatial pooling model, a useful approximation for stimuli with modest contrast. The software’s modular design provides a foundation for future extensions. We can incorporate known nonlinear properties that shape mRGC responses, including phototransduction effects [20], spatial and static nonlinearities, which often differ between ON and OFF pathways [21–24], temporal dynamics [25] and response noise [26]. Furthermore, the mRGC model is a suitable base for developing models of other types of RGCs, such as parasol and bistratified cells [27].	097
<b>1.1 Model overview</b>	098
Fig. 1 provides a model overview. Computation begins with the image spatial-spectral radiance, such as produced by a calibrated monitor. A model of the human optics, including chromatic aberrations and spectral filtering by the lens, is used to compute the retinal irradiance. Retinal irradiance is spectrally filtered by the macular pigment and then spatially and spectrally sampled by the cone photoreceptor mosaic. The parameters of the optics, macular pigment and cone mosaic all vary across the visual field, according to measurements in the literature [2].	099
The mRGC mosaic extension is composed of spatial receptive fields (RFs) whose center and surround responses are weighted sums of signals from the cone mosaic.	100
	101
	102
	103
	104
	105
	106
	107
	108
	109
	110
	111
	112
	113
	114
	115
	116
	117
	118
	119
	120
	121
	122
	123
	124
	125
	126
	127
	128
	129
	130
	131
	132
	133
	134
	135
	136
	137
	138



139  
140  
141  
142  
143  
144  
145  
146  
147  
148  
149  
150  
151  
152  
153  
**Fig. 1 Model overview.** The extant ISETBio model computes the mosaic of cone excitations.  
154 The model mRGCs are obtained by connecting their RF center and surround subregions to the cone  
155 mosaics. The connectivity matrix is constrained by anatomy and optimized through forward simulation  
156 of physiological measurements, so that the synthetic mRGCs are consistent with optical, anatomical  
157 and physiological data across the visual field.

158  
159 The wiring between the input cone mosaic and the mRGC mosaic is initially deter-  
160 mined based on anatomical constraints, such as cone and mRGC densities, and is  
161 subsequently refined using optimization algorithms that align the model's spatial RF  
162 properties with physiological measurements.

163 A key challenge is the scarcity of *in vitro* physiological data across the visual field  
164 which could be used to directly determine the wiring between the two mosaics. To  
165 address this, our framework primarily leverages more widely available *in vivo* data to  
166 derive the wiring, while validating the synthesized model against *in vitro* data where  
167 it exists. The resulting model is simultaneously consistent with cone light encoding,  
168 anatomical properties (including those of mRGCs and H1 horizontal cells), and both  
169 *in vitro* and *in vivo* physiological data. This makes the model versatile for simulating  
170 visual stimulation under *in vivo*, *in vitro*, and adaptive optics paradigms.

### 171 1.1.1 Relationship to previous computational models of RGCs

172 We are not the first to construct computational models of mammalian RGCs [28–31].  
173 Our work complements these earlier efforts, in the sense that we extend RGC mod-  
174eling in ways not captured by these models. More specifically, to our knowledge, no  
175 previous image-computable model of RGCs has attempted to realistically capture the  
176 effects of the front end encoding in the visual system, particularly the eccentricity and  
177 wavelength-varying nature of physiological optics, and the eccentricity-varying spatio-  
178 chromatic properties of the cone mosaic. Instead previous models of RGCs have either  
179 not incorporated the optics [29, 30], or employed simplified optical models [31]. Sim-  
180ilarly, previous RGC models have either not incorporated the cone mosaic [29], or  
181

182

183

184

employed simplified models of the cone mosaic [30, 31]. Finally, previous models operate on stimuli specified by achromatic light intensity rather than spectral radiance [29–31]. As such, previous models do not capture the rich spatio-chromatic interactions between stimuli and physiological optics and how their combined effects shape RGC responses. Indeed, we have recently shown that the spatio-chromatic interactions between stimuli and physiological optics can have profound effects of the response properties of midget ganglion cells [32].	185 186 187 188 189 190 191
On the other hand, previous computational models of RGCs have focused on other important components of the RGC circuit that our linear spatio-chromatic model does not address. These include processing by retinal interneurons [29–31, 33], temporal dynamics [29–31, 33], contrast grain control [28, 29], and spike generation [28–30]. These are directions that could be profitably incorporated into our modeling work, as outlined in section 4.2.2.	192 193 194 195 196 197 198
<b>1.1.2 Paper organization</b>	199
The remainder of this paper is organized as follows.	200 201
• In section 2 we describe the model’s construction stages, including, how the mRGC receptive field lattice is generated from anatomical data (section 2.1), how cones get connected to the mRGC RF centers using anatomical and physiological constraints (section 2.2), and how cone connections to mRGC RF surrounds are derived by optimizing against <i>in vivo</i> data (section 2.3).	202 203 204 205 206
• In section 3 we present, validate, and discuss first applications of the model. Specifically, we illustrate examples of synthesized mRGC mosaics (section 3.1), confirm that the model mRGC spatial RFs are consistent with <i>in vivo</i> data (section 3.2), and <i>in vitro</i> data (section 3.3), demonstrate the significant impact of physiological optics (section 3.4), and how simpler Difference-of-Gaussians models can fail to capture the true surround pooling (section 3.5). Finally we illustrate how the model can be used to estimate the contribution of the mRGC mosaic to spatiochromatic contrast sensitivity across the visual field (section 3.6).	207 208 209 210 211 212 213 214
• In section 4, we summarize our work, discuss ongoing applications of the model in its current stage, and discuss the model’s present limitations and planned expansions.	215 216 217 218 219
<b>2 Methods</b>	220 221 222 223 224 225 226 227 228 229 230
The synthesis of mRGC RF mosaics occurs in three stages. In the first stage, we generate spatial lattices representing the RF centers of cells in the mRGC mosaic and the position of cones in the cone mosaic that provides the input to the mRGC mosaic. In the second stage, we connect the input cone mosaic to the RF centers of cells in the mRGC mosaic. In the third stage, we connect the input cone mosaic to the RF surrounds of cells in the mRGC mosaic.	220 221 222 223 224 225 226 227 228 229 230

231 **2.1 Generating the spatial position lattice of mRGC RF  
232     centers (Stage 1)**

233 We begin by generating a lattice that represents the  $(x, y)$  positions of mRGC RF  
234 centers. This process comprises three sub-stages, components of which are illustrated  
235 in Fig. 2.

- 236 • **Stage 1A:** We estimate the mRGC RF center densities along the four principal  
237 meridians ( $0^\circ$ ,  $90^\circ$ ,  $180^\circ$ , and  $270^\circ$ ). These estimates are based on human data  
238 [34, 35]. We take the ON-center mRGC density to be half of the total mRGC density,  
239 ignoring the possible density differences between ON- and OFF-center mRGCs.  
240 The meridian functions are depicted in Fig. 2A.
- 241 • **Stage 1B:** We generate a continuous, two-dimensional map representing the mRGC  
242 RF density map, which is depicted in Fig. 2B. This map is created by linearly  
243 interpolating the meridian estimates, and it serves as a target for the lattice synthesis  
244 algorithm in the next stage.
- 245 • **Stage 1C:** We synthesize a sampling lattice that represents the  $(x, y)$  positions  
246 of the mRGC RF centers. The lattice is created using the iterative algorithm that  
247 we introduced in earlier work [2] for generating cone mosaics, replacing the two-  
248 dimensional cone density map with the target mRGC RF density map. A typical  
249 lattice of mRGC RF positions is obtained after about 1,300 iterations and has a  
250 density that varies smoothly over space, matching the target density, as illustrated  
251 in Figs. 2C & 2G. Example lattices of mRGC RF centers synthesized at eccentricities  
252 of  $0^\circ$  and  $20^\circ$  along the temporal horizontal meridian, are depicted in Figs. 2D &  
253 2E, respectively.
- 254

255 The same procedure is used to generate the lattice that represents the  $(x, y)$  positions  
256 of cones, using the meridian densities of cone photoreceptors in human retina [36] as  
257 targets. The density of cones in the synthesized cone lattice also varies smoothly over  
258 space and matches closely the target density, as illustrated in Figs. 2F & 2H.

260 **2.2 Connecting cones to mRGC RF centers (Stage 2)**

261 The connections between cones and mRGC centers are constrained by (1) anatomical  
262 data across the retina, specifically, the ratio of densities of mRGC RF centers to cones  
263 [34], and (2) *in-vitro* physiological data from peripheral retina, that (a) indicate that,  
264 unlike OFF-center mRGCs, which draw indiscriminately from all three cone types  
265 [15, 37, 38], ON-center mRGCs draw only from L- and M-cones, and (b) quantify  
266 the degree of RF center overlap between neighboring mRGCs [39]. The connectivity  
267 between the cone mosaic and the RF centers of the ON-center mRGC mosaic is  
268 established in 3 sub-stages, summarized here.

- 269 • **Stage 2A:** In the first substage, each L- and M-cone in the input cone mosaic  
270 gets connected to a single mRGC RF center; an mRGC RF center can receive input  
271 from more than one cone. At this substage, each connected cone has unit connection  
272 weight. S-cones are not connected because they do not contribute to ON-center  
273 mRGCs. Algorithmic details regarding this substage are provided in Supplemental  
274 Section A.1.

277  
 278  
 279  
 280  
 281  
 282  
 283  
 284  
 285  
 286  
 287  
 288  
 289  
 290  
 291  
 292  
 293  
 294  
 295  
 296  
 297  
 298  
 299  
 300  
 301  
 302  
 303  
 304  
 305  
 306  
 307  
 308  
 309  
 310  
 311  
 312  
 313  
 314  
 315  
 316  
 317  
 318  
 319  
 320  
 321  
 322

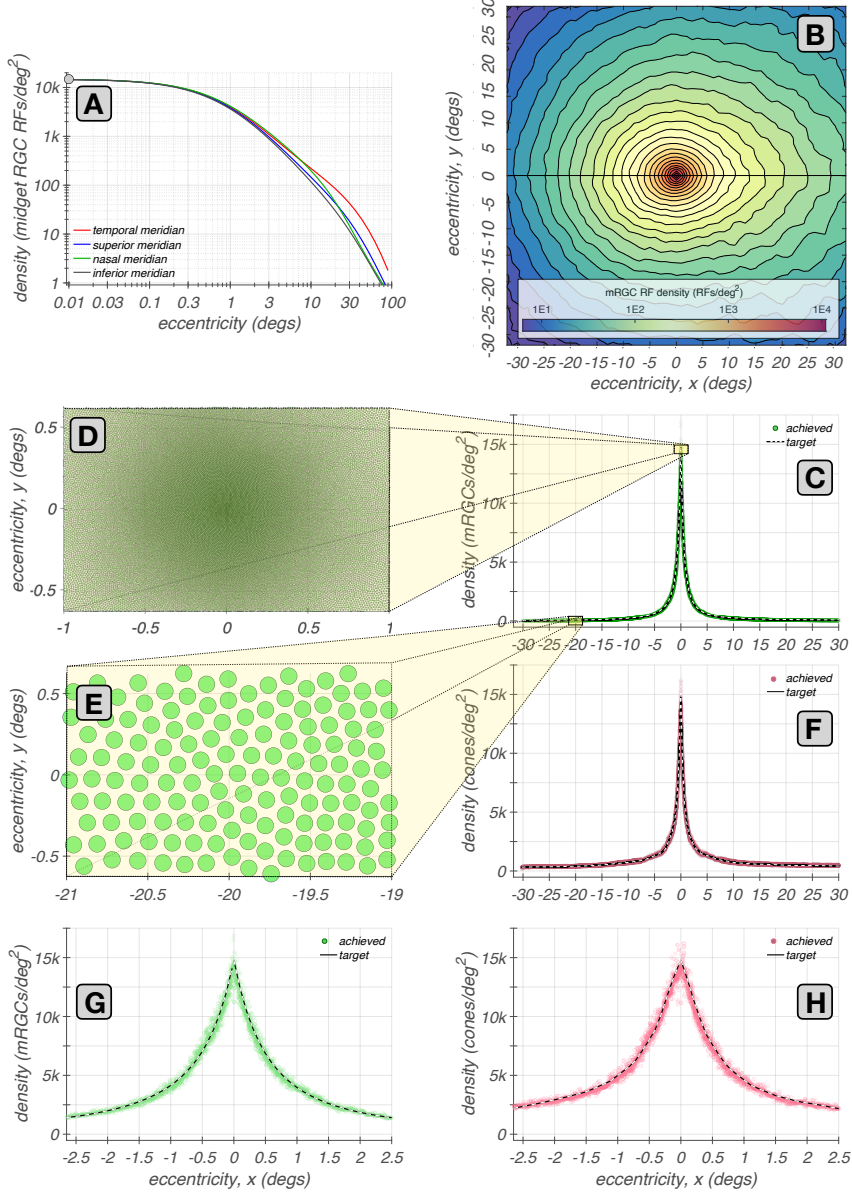


**Fig. 2 Eccentricity-varying mRGC RF position lattices.** **A:** Meridian density functions of mRGC RFs [34]. **B:** Two-dimensional mRGC RF density map obtained by interpolating the four meridian density functions. **C:** Achieved and target densities of mRGC RF centers along the horizontal meridian (green disks and white dashed line, respectively). **D & E:** Examples of  $2^\circ \times 1^\circ$  lattices of mRGC RF centers at eccentricities of  $0^\circ$  and  $20^\circ$  along the temporal meridian, respectively. **F:** Achieved and target densities of cones along the horizontal meridian (maroon disks and white dashed line, respectively). **G & H:** Achieved and target mRGC and cone densities within the central  $5^\circ$ .

323 • **Stage 2B:** The initial cone-to-RF center connectivity often results in inhomogeneities in the composition of neighboring mRGCs RF centers. These inhomogeneities are dealt with in the second substage. Here, the cone-to-RF center connections are refined to establish a balance between the spatial compactness and the spectral purity of the mRGC RF centers, which is quantified by a single parameter,  $\phi$ . For the body of this work, all mRGC mosaics are generated by maximizing spatial compactness, but the option to maximize spectral purity allows testing of different scenarios where mRGC RF centers may be biased to some extent towards cone type selective pooling [15, 16]. At this substage, cones retain their unit connection weights. Algorithmic details regarding this substage are provided in Supplemental Section A.2.

334 • **Stage 2C:** In the third substage, the mutual exclusivity constraint enforced in sub-  
335 stages 2A and 2B is lifted, and single cones are permitted to connect to multiple  
336 nearby mRGC RF centers. The extent of divergence varies with retinal eccentricity,  
337 being minimal in the fovea and increasing towards the periphery to match  
338 experimental observations [39]. This is done by varying the exponent of a supra-  
339 Gaussian distribution that describes the spatial weighting profile of cone connections  
340 to the RF centers, which at this substage, become non-binary. Algorithmic details  
341 regarding this substage are provided in Supplemental Section A.3.

342 We illustrate Stage 2 by examining key properties of synthesized mRGC RF center  
343 mosaics at each of the three substages.  
344

### 345 2.2.1 Mosaics with convergent-only cone connections (stage 2A) 346

347 Example mosaics of RF centers synthesized at four eccentricities along the temporal  
348 horizontal meridian at the end of this substage are depicted in Fig. 3, where each  
349 green ellipse represents the spatial extent of the RF center of a single mRGC. At this  
350 stage, the pooling weight of each cone is unit.

351 For the foveal mosaic depicted in Fig. 3A, RF centers connect to just a single cone.  
352 Note how RF center sizes increase as we move towards parafoveal regions to the left  
353 and right sides of Fig. 3A. This is due to the continuously increasing, with eccentricity,  
354 cone aperture in the input cone mosaic. The empty regions in this foveal mRGC RF  
355 center mosaic correspond to the location of S-cones which are not pooled by the model.

356 In the parafoveal mosaic depicted in Fig. 3B, RF centers mostly receive inputs  
357 from two cones, whereas in the more peripheral mosaics depicted in Figs 3C & 3D,  
358 RF centers connect to multiple cones. Note that the number of cones connecting to  
359 RF centers does not correspond precisely to RF center size, because cone aperture  
360 and inter-cone spacing both increase with eccentricity. At all eccentricities, however,  
361 mRGC RF center mosaics tile the retinal space with no spatial overlap or voids, except  
362 at the sparse positions where S-cones are located.

363  
364  
365  
366  
367  
368

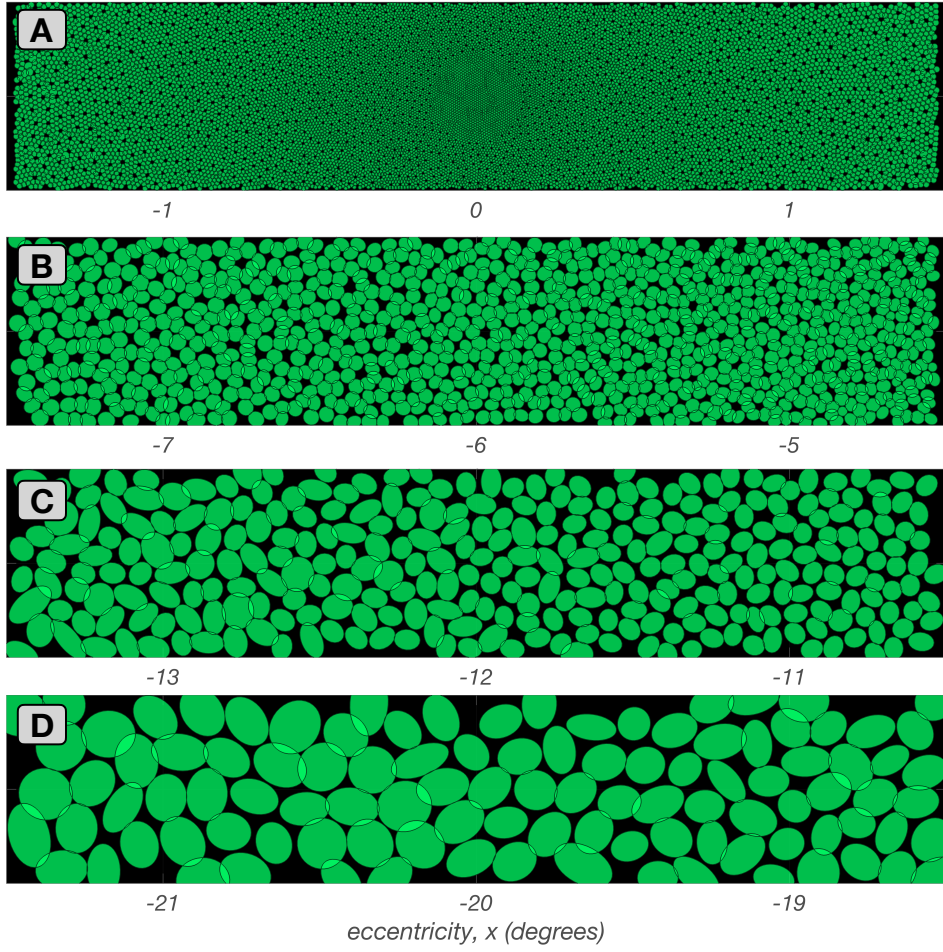


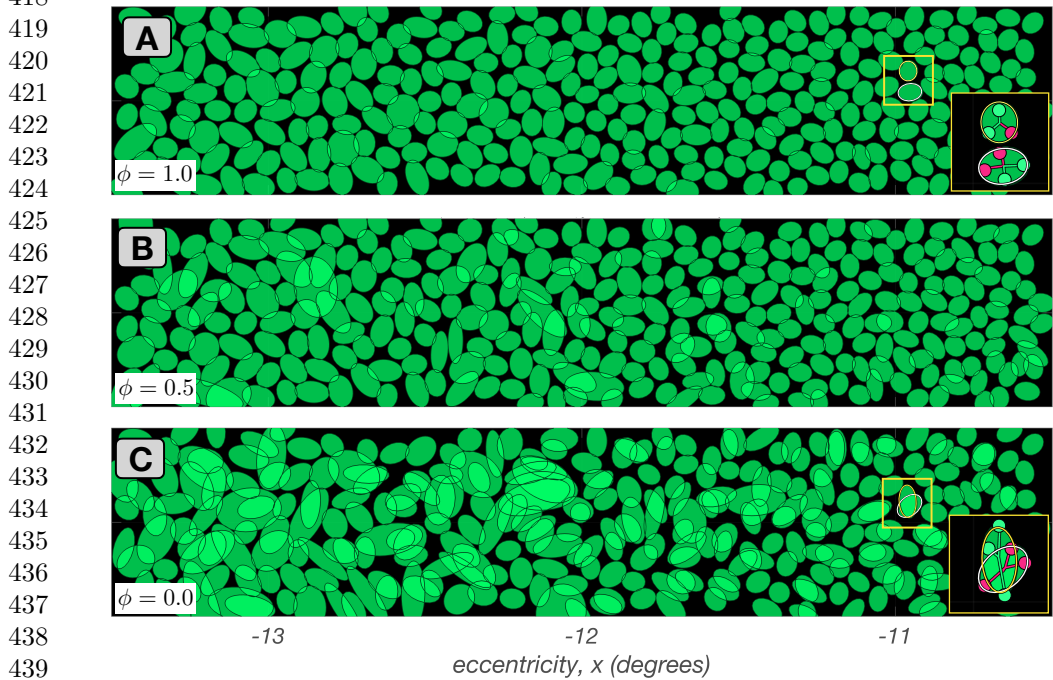
**Fig. 3 Stage 2A mRGC RF mosaics.** Each panel shows a  $3.0^\circ \times 0.5^\circ$  mosaic of synthesized mRGC RF centers at a different visual field location from fovea to periphery. The green ellipses depict the spatial region that encompasses all cones pooled by single RF centers. **A:** Foveal mosaic, in which RF centers receive signals from a single L- or M-cone. **B:** Mosaic centered at  $6.0^\circ$  along the temporal horizontal meridian, in which RF centers receive signals from 2–3 L/M-cones. **C:** Mosaic centered at  $12.0^\circ$  along the temporal horizontal meridian, in which RF centers receive signals from 3–4 L/M-cones. **D:** Mosaic centered at  $20.0^\circ$  along the temporal horizontal meridian, in which RF centers receive signals from 6–9 cones.

### 2.2.2 Mosaics synthesized under different spatial compactness/spectral purity tradeoffs (stage 2B)

This substage allows for different optimizations of cone pooling within the mRGC RF centers, which is controlled by the spatial compactness/spectral purity tradeoff parameter,  $\phi$ . At this stage, the pooling weight of each cone is still set to unit, independent of the value of  $\phi$ .

369  
370  
371  
372  
373  
374  
375  
376  
377  
378  
379  
380  
381  
382  
383  
384  
385  
386  
387  
388  
389  
390  
391  
392  
393  
394  
395  
396  
397  
398  
399  
400  
401  
402  
403  
404  
405  
406  
407  
408  
409  
410  
411  
412  
413  
414

415 Fig. 4 depicts examples of mRGC RF center mosaics all synthesized at  $12^\circ$  along  
 416 the temporal meridian, but under different values of  $\phi$ . Fig. 4A depicts the mosaic  
 417



441 **Fig. 4 Mosaics of mRGC RF centers at the end of stage 2B.** Depicted here are  $3.0^\circ \times 0.5^\circ$   
 442 mRGC mosaics, each centered at  $12^\circ$  along the temporal horizontal meridian, but synthesized under  
 443 different values of tradeoff between spatial compactness and spectral purity,  $\phi$ . **A:**  $\phi = 1.0$  (maximal  
 444 spatial compactness). **B:**  $\phi = 0.5$ . **C:**  $\phi = 0$  (maximal spectral purity). Insets in A and C depict  
 445 pooling of cones within the RF centers of the two neighboring mRGCs contained within the yellow  
 446 square. The inset in C illustrates how RF center overlap and spatial disorder is introduced as the  
 447 algorithm avoids cones of different types that are close to the RF center in order to maximize the  
 448 spectral purity of RF centers.

449 synthesized under  $\phi = 1$ , where spatial compactness is maximal and spectral purity  
 450 constraint is not enforced. Note that the RF centers tile the visual field relatively uni-  
 451 formly with no overlap. Figures 4B and 4C depict mosaics synthesized as  $\phi$  decreases  
 452 to 0.5 and 0.0, respectively, which increasingly enforces center connections to cones of  
 453 the same type. Note that this occurs at the cost of reduced spatial compactness, as is  
 454 evident by the increased spatial disorder and overlap in the RF centers.

455 By varying  $\phi$  we can examine the effect that cone-selective pooling may have on  
 456 mRGC RF spatial structure, as well as on the spatio-chromatic processing in the  
 457 mRGC pathway. Current electrophysiological evidence in peripheral mRGCs RF cen-  
 458 ters favors little selective cone pooling [15, 16, 40], i.e., a  $\phi$  value of  $\approx 1$ . However, the  
 459 degree of cone type selectivity in more central locations is not known with as much  
 460

certainty. For example, there is anatomical evidence that ON-center mRGCs in the fovea contact multiple ON-cone bipolars, as opposed to OFF-center mRGCs, which contact single OFF-cone bipolars [41], and also electrophysiological evidence that the RF centers of parafoveal mRGCs appear to be pooling from more than one cones [42]. In general, the question of whether foveal mRGCs that pool from more than one cone in their RF centers are doing so selectively remains unanswered. Our modeling approach allows exploration of the benefits and tradeoffs of cone-selective pooling at any retinal eccentricity, although we do not pursue such exploration in this paper.

### 2.2.3 Mosaics with divergent cone connections (stage 2C)

In the final substage of establishing the wiring between mRGC RF centers and the input cone mosaic, the mutual exclusivity constraint is lifted and single cones are permitted to connect to multiple nearby mRGC RF centers. This divergence of cone connections is enabled by replacing the binary distribution of cone pooling weights in the mRGC RF centers with a supra Gaussian distribution, as illustrated in Fig. 5.

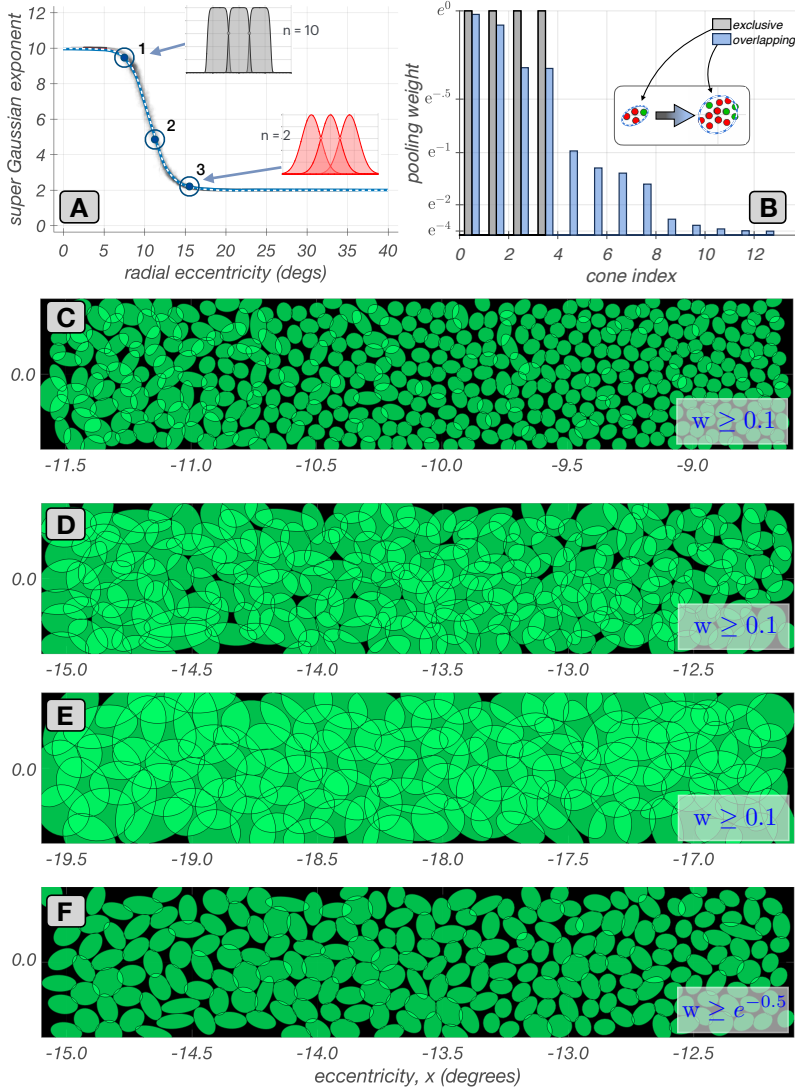
Fig. 5A depicts how a progressively increasing overlap in neighboring mRGC RF centers with eccentricity is accomplished by varying the exponent of the supra-Gaussian distribution. In central retina, the exponent is kept at 10, which results in a flat top distribution of weights with minimal overlap between neighboring RF centers (gray histograms in the inset of Fig. 5A). As eccentricity increases beyond 7°, the exponent decreases and asymptotes to a value of 2 at around 15°, which results in Gaussian distributions of weights and a significant overlap between neighboring RF centers (red histograms in the inset of Fig. 5A).

To our knowledge, there is no physiological data on the variation with eccentricity of the divergence of cone connections to nearby mRGC RF centers. We implemented the eccentricity varying exponent as a way to smoothly bridge the gap between the fovea, where midget RF centers receive a single cone input [41, 42], and data available for the periphery, where the degree of mRGC RF overlap has been characterized [39].

The transformation of cone pooling weights from binary and mutually exclusive to graduated and shared is depicted in Fig. 5B for an mRGC located at an eccentricity of 12°, with gray and blue histograms depicting the spatial distributions of cone pooling weights before and after, respectively, substage 2C.

Figs. 5C–5E depict mosaics with divergent connections synthesized at three eccentricities. In these mosaic depictions, each green ellipse represents the spatial extent that encompasses all cones that are pooled by the RF center of a single mRGC with weights  $\geq 0.1$ . For the mosaic centered at 10° (Fig. 5C), divergence of cone connections has just begun. The overlap in RF centers due to the divergence of connections increases as we move in eccentricity from 9° on the right side to 11°, on the left side. For the mosaic centered at around 13° (Fig. 5D), cone divergence and RF center overlap is higher and again increases with increasing eccentricity. For the mosaic centered at around 18° (Fig. 5E), divergence of cone connections has asymptoted, and we have a constant RF center overlap.

Finally, Fig. 5F provides a visualization comparable to the visualization commonly reported by *in vitro* RF mapping studies [39]. It depicts the same mosaic as Fig. 5D,



542 **Fig. 5 Mosaics of mRGC RF centers with divergent cone connections (stage 2C).**  
543 **A:** Variation with eccentricity of the exponent of the supra-Gaussian distribution of cone pooling  
544 weights in mRGC RF centers. The exponent is set to 10 in the central retina, resulting in flat top  
545 weight distributions with zero overlap (gray histograms). As eccentricity is increased, the exponent  
546 is gradually decreased, achieving a value of 2.0, at around 15° (red histograms). **B:** Transformation  
547 of cone pooling weights, from binary, in mutually exclusive connections, (gray histogram) to non-  
548 binary in shared cone connections, (blue histogram) due to the supra-Gaussian distribution for an  
549 example mRGC. Insets depict the spatial arrangement of cones that are connected with binary and  
550 non-binary weights. **C, D & E:** Mosaics at 10°, 13°, and 18°, respectively, along the temporal  
551 horizontal meridian with divergent cone connections. The RF center ellipses encompass the ensemble  
552 of cones with pooling weights  $\geq 0.1$ . **F:** Same mosaic as **C**, but with ellipses showing cones with  
553 pooling weights  $\geq e^{-0.5}$ .

but with ellipses encompassing cones that are pooled with weights  $\geq e^{-1/2} \approx 0.67$ .  
This depiction choice makes the overlap less visually salient. 553  
554  
555

## 2.3 Connecting cones to mRGC RF surrounds (Stage 3) 556

### Overview 557

In the last stage of mRGC mosaic synthesis, we derive the cone pooling weights for the mRGC RF surrounds. Since there are no clear anatomical data on surround sizes, these weights are determined using *in vivo* characterizations of macaque mRGC visual space-referred spatial transfer functions, vSTF( $\omega$ ), i.e., the variation in response amplitude of mRGC cells as a function of stimulus spatial frequency,  $\omega$ . We use the characterizations of Croner & Kaplan [17], who measured vSTF( $\omega$ ) for populations of mRGCs across a wide range of eccentricities. 558  
559  
560  
561  
562  
563  
564  
565

We incorporate these data into the model using numerical optimization. More specifically, we determine the cone-to-mRGC RF surround connections such that a forward simulation of the *in vivo* physiological experiments of Croner & Kaplan through the model best reproduces the experimental data. This approach allows us to use data collected through physiological optics, which blur the stimulus in an eccentricity and wavelength dependent manner, to determine the wiring of cones to mRGC RF surrounds across eccentricities. 566  
567  
568  
569  
570  
571  
572

Importantly, the optimization is achieved while adhering to the connectivity between the cone mosaic and mRGC RF centers established in stage 2. Simultaneously, the parametric form of the spatial distribution of the surround weights is constrained based on Packer & Dacey's characterizations of the spatial RF of macaque H1 horizontal cells [43], which are the main components of the linear spatial mRGC RF surrounds [44]. The use of optimization around forward simulation of an experiment to integrate data from multiple non-commensurate sources is an important innovation of our RGC modeling approach. Stage 3 proceeds in three sub-stages. 573  
574  
575  
576  
577  
578  
579  
580  
581

- **Stage 3A:** We begin by computing the visual space-referred cone mosaic responses to stimuli used to measure vSTFs in macaque mRGCs. This is done by presenting achromatic gratings of different spatial frequencies which are delivered to the retina through human physiological optics [45]. We use human optics as a proxy of how macaque optics would have blurred the stimuli employed by the *in vivo* characterizations of Croner & Kaplan [17], which were collected with stimuli viewed through the animal's natural optics. 582  
583  
584  
585  
586  
587  
588
- **Stage 3B:** We derive surround cone pooling functions for a subset of target synthetic mRGCs, which span the extent of the synthesized mRGC mosaic. This optimization is done so that the ensuing target cells have (a) vSTF characteristics that are well approximated by a Difference of Gaussians (DoG) model, with (b) parameters of the DoG model reasonably matching the DoG model parameters reported by Croner & Kaplan for macaque mRGCs at corresponding eccentricities, while (c) their surround cone pooling weights maintain macaque H1-like spatial properties as characterized by Packer & Dacey. 589  
590  
591  
592  
593  
594  
595  
596
- **Stage 3C:** We compute surround cone pooling weights for all cells in the synthesized mRGC mosaic by evaluating the derived surround cone pooling functions at 597  
598

599 the vicinity of each mRGC's input cone mosaic and subsequently interpolating the  
600 weights computed by the different pooling functions. A small amount of jitter in  
601 the ratio of the surround to center weights is added to simulate the variance in  
602 integrated surround to center ratios seen in the macaque data.

603

604 **2.3.1 Computation of visual space-referred cone mosaic responses**  
605 **to stimuli used to measure vSTFs in macaque mRGCs**  
606 **(Stage 3A)**

607

608 We employ the ISETBio machinery to compute the excitation of the input cone mosaic  
609 to achromatic gratings of different spatial frequencies delivered to the retina via phys-  
610 iological optics. This process captures several crucial spatio-chromatic effects in the  
611 transformation of scene radiance into cone responses: spatial and chromatic filtering  
612 by physiological optics, spectral filtering by the eye's inert pigments, and sampling by  
613 the interdigitated trichromatic cone mosaic. To mimic the phototransduction process,  
614 cone excitation responses are converted to cone modulation responses.

615 In these computations, we employ human physiological optics matched to the  
616 eccentricity of each synthesized mRGC, but we adjust the defocus term of the modeled  
617 optics so as to maximize the Strehl ratio. The Strehl ratio is defined as the ratio of peak  
618 sensitivity of the optical point spread function (PSF) at the wavelength of focus, here  
619 550 nm, to the peak sensitivity of a diffraction-limited PSF. This is done as a proxy to  
620 the experimental paradigm of Croner & Kaplan, in which corrective lenses were used  
621 to maximize cell responses at high spatial frequencies (personal communication with  
622 the late Ehud Kaplan).

623

624 **2.3.2 Deriving surround cone pooling functions for a subset of**  
625 **target synthetic mRGCs (Stage 3B)**

626 Croner & Kaplan reported summaries of the spatial RF characteristics across pop-  
627 ulations of mRGCs by measuring their vSTF and then fitting a DoG model to the  
628 measured vSTF. The DoG model defined in the spatial frequency,  $\omega$ , domain is given  
629 by:

$$630 \text{DoG}(\omega) = K_c \cdot R_c^2 \cdot \exp[-\pi \cdot R_c \cdot \omega]^2 - K_s \cdot R_s^2 \cdot \exp[-\pi \cdot R_s \cdot \omega]^2 \quad (1)$$

631 where  $K_c$  and  $K_s$  are the peak sensitivities of the RF center and RF surround  
632 mechanisms, and  $R_c$  and  $R_s$  are the corresponding characteristic radii.  
633

634 The vSTF of a typical macaque mRGC is depicted in Fig. 6A with cyan disks. The  
635 solid heavy line depicts the fitted DoG model, with its center and surround components  
636 depicted by the thin solid and dashed lines, respectively. The shape of the vSTF is  
637 determined by two key measures, the ratio of surround to center characteristic radii,  
638  $R_s/R_c$ , and the ratio of surround to center integrated sensitivities,  $K_s/K_c \times (R_s/R_c)^2$ .  
639 The distributions of these two ratios as a function of eccentricity in the population of  
640 mRGCs recorded by Croner & Kaplan are depicted by the gray squares in Figs 6B1  
641 & 6B2. The mean variation in these two ratios, shown as dashed lines, are the target  
642 values used to derive the surround cone pooling weights in the synthetic mRGCs.

643 The optimization process of deriving the mRGC RF surround cone pooling func-  
644 tions is illustrated schematically in Fig. 6C. The vSTF of the target synthetic mRGC

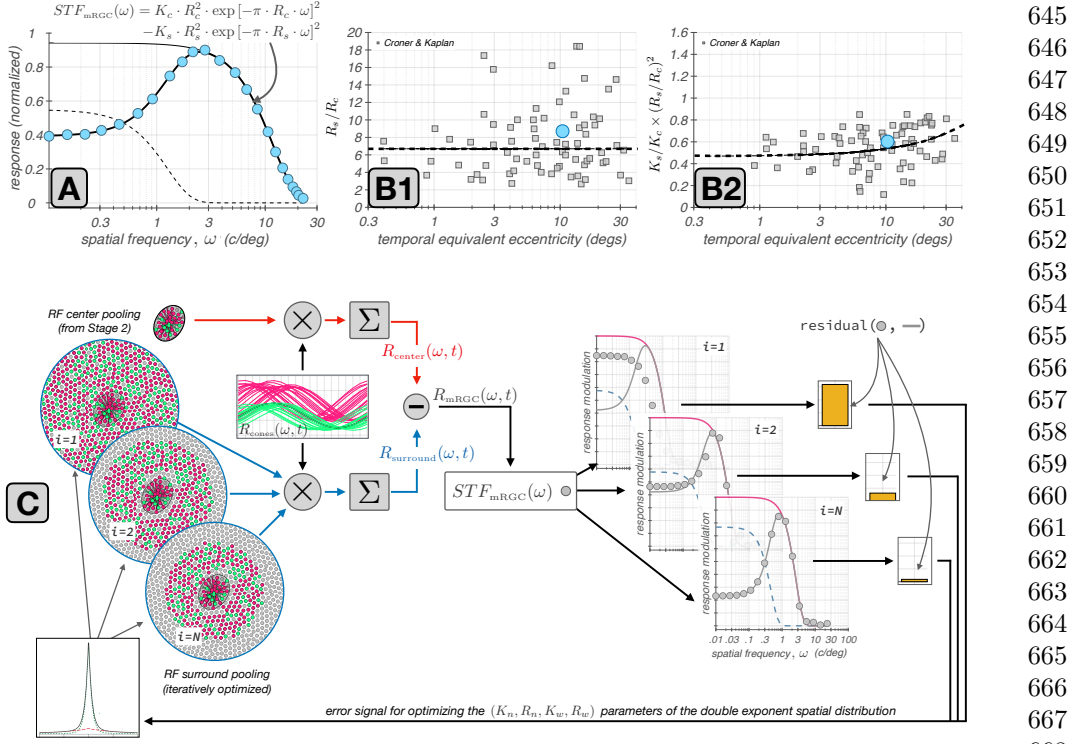


**Fig. 6 Derivation of cone weights to mRGC surrounds by forward simulation of the Croner & Kaplan vSTF measurements.** **A:** Typical macaque mRGC vSTF (cyan disks) fitted with a Difference of Gaussians model (thick black line). The model's center and surround components are depicted by the thin black and the dashed line, respectively. **B1 & B2:** Ratios of surround to center characteristic radii,  $R_s/R_c$ , and ratios of surround to center integrated sensitivities,  $K_s/K_c \times R_s^2/R_c^2$  as a function of eccentricity in the population of mRGCs recorded by Croner & Kaplan [17]. The dashed lines represent the trends in these two ratios as a function of eccentricity. The cyan disks depict the ratios for the example vSTF depicted in A. **C:** Depiction of the iterative estimation of surround cone pooling weights in synthetic mRGCs by forward simulation of the Croner & Kaplan vSTF measurements. See description in text for more details.

is computed by forward simulation of the experiment of Croner & Kaplan. The time course of responses of L- and M-cones in the input cone mosaic to a drifting grating stimulus of spatial frequency  $\omega$ ,  $R_{\text{cones}}(\omega, t)$ , computed in Stage 3A, are depicted by the red and green traces in the rectangular panel of Fig. 6C. A spatially weighted sum of these cone responses using the RF center cone pooling weights computed in Stage 2, is used to compute the response of the RF center,  $R_{\text{center}}(\omega, t)$ . This operation, which is depicted by the red computation arm in Fig. 6C, is fixed throughout the optimization of the surround.

To compute the spatial distribution of surround cone pooling weights we impose a parametric form that is described by the sum of a narrow and a wide exponential spatial component, based on characterizations of the spatial RF properties of H1

645  
646  
647  
648  
649  
650  
651  
652  
653  
654  
655  
656  
657  
658  
659  
660  
661  
662  
663  
664  
665  
666  
667  
668  
669  
670  
671  
672  
673  
674  
675  
676  
677  
678  
679  
680  
681  
682  
683  
684  
685  
686  
687  
688  
689  
690

691 horizontal cells by Packer & Dacey [43]. Specifically,

692

$$693 \quad W_s(r) = K_{\text{wide}} \times \exp[-r/R_{\text{wide}}] + K_{\text{narrow}} \times \exp[-r/R_{\text{narrow}}] \quad (2)$$

694

695 where  $r$  is the radial distance from the RF center,  $K_{\text{wide}}$  and  $K_{\text{narrow}}$  are the peak sen-  
696 sitivities of the wide and the narrow components, respectively, and  $R_{\text{wide}}$  and  $R_{\text{narrow}}$   
697 are the corresponding characteristic radii.

698 Beginning with a random initial value for the parameters of the double exponential  
699 distribution, we compute an initial estimate of the surround cone weights by eval-  
700 uating  $W_s(r)$  at the vicinity of the input cone mosaic that surrounds the RF center.  
701 These weights are depicted in the top-left circular panel of Fig. 6C (labeled as  $i = 1$ ,  
702 with  $i$  denoting iteration). Using these initial weights we compute a weighted sum of  
703 the surround cone responses to derive the initial estimate of the surround response,  
704  $R_{\text{surround}}(\omega, t)$ . This operation is depicted by the blue computation arm in Fig. 6C.

705 The composite response of the synthesized mRGC is obtained by instantaneously  
706 subtracting the surround response from the center response:

707

$$708 \quad R_{\text{mRGC}}(\omega, t) = R_{\text{center}}(\omega, t) - R_{\text{surround}}(\omega, t) \quad (3)$$

709

710 The amplitude modulation of  $R_{\text{mRGC}}(\omega, t)$  is taken as the value of the synthesized  
711 cell's visual space-referred STF,  $\text{vSTF}_{\text{mRGC}}(\omega)$ . Repeating over a range of spatial  
712 frequencies, we obtain the initial estimate of the full  $\text{vSTF}_{\text{mRGC}}$ , which is depicted by  
713 the gray disks in the top-right rectangular panel of Fig. 6C, labeled as  $i = 1$ .

714 Following the experimental procedure of Croner & Kaplan, we fit the computed  
715  $\text{vSTF}_{\text{mRGC}}(\omega)$  with a DoG model. The DoG fit is depicted by the solid gray line in  
716 the top-right rectangular panel of Fig. 6C. Note that in this procedure we constrain  
717 the DoG model fit so that its shape parameters,  $R_s/R_c$ , and  $K_s/K_c \times R_s^2/R_c^2$ , both  
718 lie within a narrow range of the mean values of the  $R_s/R_c$ , and  $K_s/K_c \times R_s^2/R_c^2$   
719 ratios reported for macaque mRGCs at corresponding eccentricities [17]. Due to this  
720 constrain, in the first iteration the residual between the computed  $\text{vSTF}_{\text{mRGC}}$  and the  
721 DoG model fit to it, is large.

722 This residual,  $\|\text{vSTF}_{\text{mRGC}} - \text{DoG}\|$ , which is depicted by the yellow bar in the  
723 right-most panel of Fig. 6C, serves as an error signal for the optimization of surround  
724 weights. The algorithm minimizes this error signal by adjusting the parameters of  
725  $W_s(r)$ , which controls the surround weights. This adjustment is also constrained, so  
726 that the parameters of  $W_s(r)$  remain within a range of the values reported in macaque  
727 H1 horizontal cells [43].

728 When the  $\|\text{vSTF}_{\text{mRGC}} - \text{DoG}\|$  reaches a minimum value, at iteration  $i = N$   
729 in Fig. 6C, we obtain the optimized surround cone pooling function for the target  
730 synthetic mRGC. Additional details about this surround optimization method are  
731 provided in Supplemental Section B.1.

732  
733  
734  
735  
736

## 2.4 Deriving surround cone pooling weights for each cell in the mosaic(stage 3C)

The optimization of the surround cone pooling functions is a computationally expensive process. It is therefore conducted on a sparse spatial grid (with  $N_{xy}$  nodes), which encompasses the spatial extent of the synthesized mRGC mosaic. At each node of the spatial grid, we determine the range of cone numerosities in the RF centers of nearby synthetic mRGCs, and we derive optimized surround cone pooling functions for each of the encountered RF center cone numerosities ( $N_c$ ), and we do this twice, once for L-cone dominated RF centers, and once for M-cone dominated RF centers.

Once these  $N_{xy} \times N_c \times 2$  surround cone pooling functions are derived, we compute surround cone pooling weights for all synthetic mRGCs. For each synthetic mRGC we determine the 3 nearest spatial grid nodes, and extract the optimized surround cone pooling functions that were derived at this node for the cone numerosity that matches that of the examined mRGC, for both L- and M-cone RF center dominance variants. Then we evaluate the six optimized surround pooling functions at the input cone mosaic in the vicinity of the examined mRGC, deriving six sets of surround cone pooling weights. The examined cell's surround cone pooling weights are determined by interpolating the 6 sets of weights spatially, weighted inversely proportionally by the distance between the location of the examined mRGC and the location of the optimized model, and spectrally, weighted based on the relative L-/M-cone weight ratio in the RF center of the examined mRGC.

### 2.4.1 Adjusting the surround pooling variance

The final step in the generation of the mRGC RF surrounds is to apply a noisy scalar multiplier to all surround pooling weights of individual mRGCs. The value of this scalar is chosen so that the variance in the ratio of surround to center integrated sensitivities,  $K_s/K_c \times (R_s/R_c)^2$ , of the synthetic mRGCs matches the variance observed in the population of macaque mRGCs recorded by Croner & Kaplan at the corresponding eccentricity. The manipulation in  $K_s/K_c \times (R_s/R_c)^2$  variance does not require re-computing the surround pooling functions. This is unlike manipulating the variance in the  $R_s/R_c$  ratio, which requires re-computing the surround pooling functions.

## 2.5 Computing mRGC responses from cone mosaic responses

A fully synthesized mRGC mosaic consists of two connectivity matrices:  $P_{\text{center}}(i, k)$ , determined in synthesis stage 2, and  $P_{\text{surround}}(i, k)$ , determined in synthesis stage 3, which capture the weights by which the RF center and the RF surround mechanisms, respectively, of the  $k^{\text{th}}$  cell in the mRGC mosaic pools signals from the  $i^{\text{th}}$  cone in the input cone mosaic.

Since the current version of the mRGC model does not contain a temporal component, the response of the  $k^{\text{th}}$  mRGC to some stimulus at time instant,  $t$ ,  $R_{\text{stim}}(k, t)$ , is computed instantaneously by weighting the response of the input cone mosaic to that

737  
738  
739  
740  
741  
742  
743  
744  
745  
746  
747  
748  
749  
750  
751  
752  
753  
754  
755  
756  
757  
758  
759  
760  
761  
762  
763  
764  
765  
766  
767  
768  
769  
770  
771  
772  
773  
774  
775  
776  
777  
778  
779  
780  
781  
782

783 stimulus at time  $t$ ,  $C_{\text{stim}}(:, t)$ , as follows:

784

$$785 \quad R_{\text{stim}}(k, t) = \frac{1}{\sum_{i=1}^n P_{\text{center}}(i, k)} \times \dots \\ 786 \\ 787 \\ 788 \\ 789 \\ 790 \\ 791 \quad \left( \sum_{i=1}^n P_{\text{center}}(i, k) \cdot C_{\text{stim}}(i, t) - \sum_{j=1}^m P_{\text{surround}}(j, k) \cdot C_{\text{stim}}(j, t) \right) \quad (4)$$

792 To mimic adaptation to the background stimulus, synthetic mRGCs typically operate  
793 on cone contrast responses, instead of cone excitation responses, so the  $C_{\text{stim}}(i, t)$   
794 term in the above equation is computed as:

795

$$796 \quad C_{\text{stim}}(i, t) = \frac{E_{\text{stim}}(i, t) - E_{\text{bkgnd}}(i)}{E_{\text{bkgnd}}(i)} \quad (5) \\ 797 \\ 798$$

799 where  $E_{\text{stim}}(i, t)$  is the excitation response of the  $i^{\text{th}}$  cone to the examined stimulus at  
800 time  $t$ , and  $E_{\text{bkgnd}}(i)$  is that cone's excitation response to a uniform field, zero contrast  
801 stimulus, whose mean chromaticity and luminance match those of the examined  
802 stimulus.

803

## 804 2.6 Equating eccentricity across human and macaque retina

805

806 We have built our model to describe human retina, but some of the fundamental  
807 physiological data available to constrain the model [17], and to validate the model  
808 [15, 17, 46], exists only for macaque monkey. To integrate and/or contrast data between  
809 human and macaque, we need to equate retinal eccentricity across the two species.  
810 We compared how measurements of cone density in the two species [36, 47] align  
811 when plotted in terms of millimeters of retina versus plotted in terms of visual angle.  
812 We observed better, although not perfect, alignment when eccentricity was specified  
813 in terms of millimeters of retina, and thus chose to align monkey to human data by  
814 equating millimeters of retina. More specifically, to determine the equivalent macaque  
815 angular eccentricity of a synthetic human RGC we first convert the angular eccentricity  
816 of the human RGC into its linear eccentricity (in retinal millimeters) using  
817 the formula derived by Watson [34] based on the wide-angle schematic eye model of  
818 Drasdo & Fowler [48]. We then assume that macaque and human linear eccentricities  
819 are identical, and finally, convert the macaque linear eccentricity into its correspond-  
820 ing angular eccentricity (in degrees of visual angle), assuming a retinal magnification  
821 factor of 221  $\mu\text{m}/\text{deg}$  for the macaque eye [49].

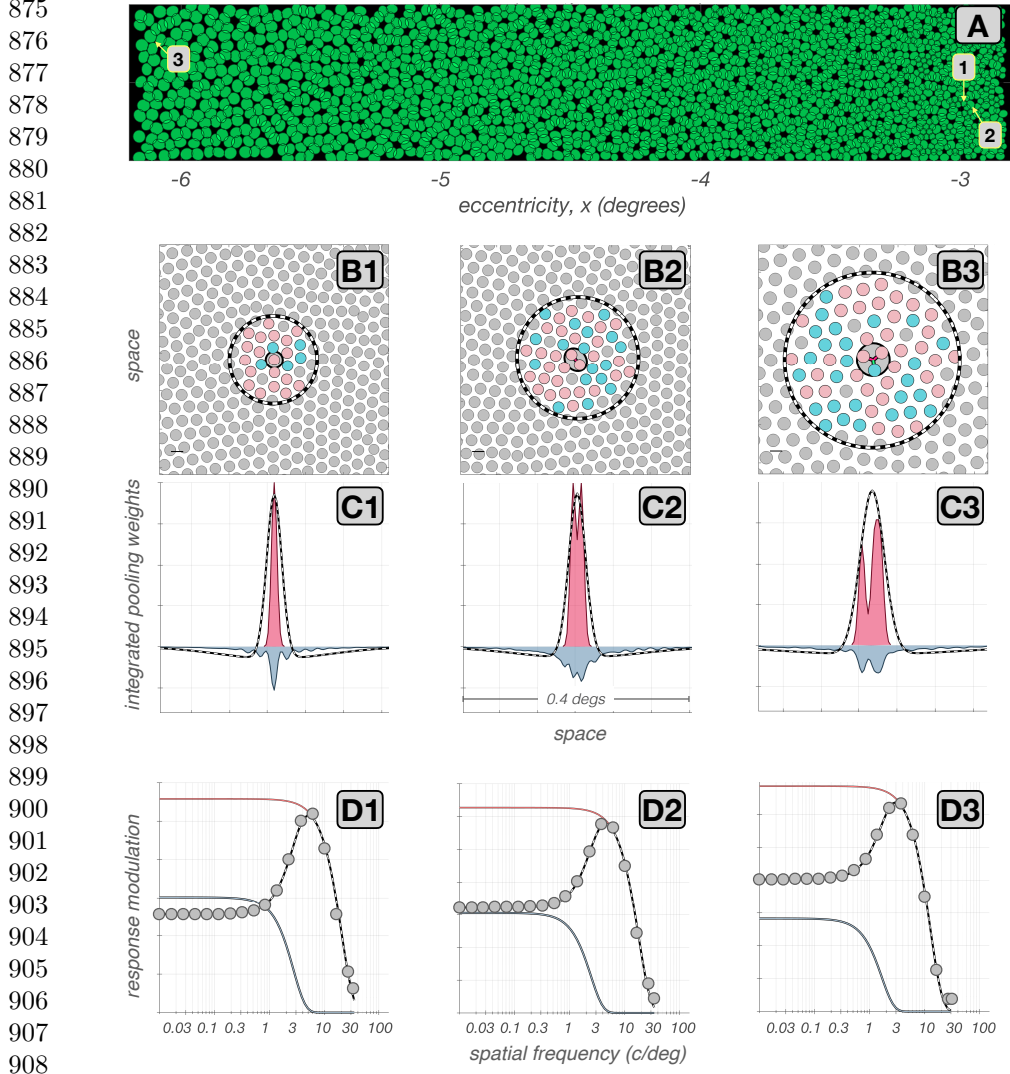
822

## 823 3 Results

824

825 A key feature of our model is its dual representation of mRGC receptive field (RF)  
826 properties, which separates neural circuitry from optical effects. The first representa-  
827 tion, in *retinal space*, models the direct pooling of cone signals by the RF center and  
828 the RF surround. This describes the cell's intrinsic spatio-chromatic filtering and is

directly comparable to anatomical data and physiological measurements that bypass the eye's optics (e.g., <i>in vitro</i> or adaptive optics experiments [10, 50]). In contrast, the second representation, in <i>visual space</i> , models the end-to-end processing of a stimulus as it passes through the eye's optics to the mRGC mosaic. This representation is applicable to conventional <i>in vivo</i> physiology and psychophysical assessments of visual function.	829 830 831 832 833 834
The ability to go back and forth between cone and visual space is critical to understanding how retinal cone pooling interacts with physiological optics to generate the processing characteristics of cells in visual space, which is what ultimately determines natural visual performance. This ability is also critical in interpreting results from <i>in vivo</i> physiology in terms of the underlying retinal wiring [32], as well as to relating results obtained under adaptive optics viewing conditions to results obtained under natural viewing conditions [10].	835 836 837 838 839 840 841
In this section we illustrate and contrast spatial RF characteristics of synthetic mRGCs in the two representations and validate the properties of synthetic mRGCs against those of macaque mRGCs as characterized by <i>in vivo</i> and <i>in vitro</i> physiological studies.	842 843 844 845 846
<b>3.1 Spatial characteristics of synthesized mRGC receptive fields</b>	847 848 849
Spatial characteristics of cells in an mRGC mosaic synthesized at $4.5^\circ$ along the temporal horizontal meridian are depicted in Fig. 7. Fig. 7A depicts the mosaic together with numbered positions which identify the locations of three selected cells whose spatial RF characteristics are explored in detail.	850 851 852 853
Figs. 7B1–7B3 depict the cone pooling maps of the selected cells. Here, pink and cyan disks depict L- and M-cones, respectively, with RF center pooling weights $\geq 0.1$ , or with RF surround pooling weights $\geq 0.005$ , whereas gray disks depict cones that are either not pooled at all or pooled with a weight less than the threshold for labeling. The solid and dashed lines depict the spatial pooling extents of the RF center and surround mechanisms, respectively.	854 855 856 857 858 859
The cell depicted in Fig. 7B1 is located at an eccentricity of $3^\circ$ . Its RF center pools from a single L-cone and its RF surround pools from a total of 16 L- and M-cones. The cell depicted in Fig. 7B2, also located at $3^\circ$ , pools from two L-cones in its RF center, and its RF surround is larger, pooling from 44 L- and M-cones. The cell depicted in Fig. 7B3 is located at $6^\circ$ . Its RF center, which pools from 2 L-cones and 1 M-cone, and its RF surround are both larger than those of the first 2 cells. The cone pooling maps depicted in Figs 7B1–7B3 illustrate the spatial connectivity between the input cone mosaic and the center and surround subregions of mRGC RFs, but do not depict the strength of these connections. In this sense, these maps depict the type of information that is available from detailed anatomical studies.	860 861 862 863 864 865 866 867 868 869
Figs 7C1–7C3 add to this view by providing information about the strength of the cone inputs in these exemplar cells. Here, the maroon and slate histograms depict the cells' spatially integrated (along the y-axis) cone pooling weights for the RF center and the RF surround mechanisms, respectively. Note that in the cell depicted in Fig. 7C1, the double exponential spatial profile of the surround cone pooling mechanism, with	870 871 872 873 874



909 **Fig. 7 Spatial RF characteristics of synthetic mRGCs** **A:** Mosaic of RF centers of an mRGC  
910 mosaic synthesized at  $4.5^\circ$  along the temporal horizontal meridian. **B1–B3:** Cone pooling maps for  
911 three exemplar cells whose positions within the mRGC mosaic are labeled in A. Pink and cyan disks  
912 depict L- and M-cones, respectively, with RF center pooling weights  $\geq 0.1$ , or with RF surround  
913 weights  $\geq 0.005$ . Gray disks represent either S-cones, which are not pooled in our model, or L-/M-  
914 cones with pooling weights lower than the labeling thresholds. The solid and dashed black lines depict  
915 the extents of the RF center and surround pooling regions. **C1–C3:** Y-axis integrated cone pooling  
916 weight profiles of the RF center (maroon) and the RF surround (slate) mechanisms. The dashed lines  
917 depict the visual space-referred line weighting functions as derived by fitting Difference of Gaussians  
918 (DoG) models to each cell's vSTF. **D1–D3:** The vSTFs of the exemplar mRGCs, computed under  
919 physiological optics, are depicted by the gray disks. The gray lines depict the DoG model fits to  
920 these vSTFs, and the maroon and slate lines depict the models' center and surround components,

a sharp peak around the RF center and more shallow weights in peripheral regions, is  
prominent. In the two other cells shown, this feature is less prominent. 921  
922

This observation, where cells with larger RF centers have less peaked surround  
weights than cells with smaller RF centers is seen commonly in our synthetic mRGCs.  
The variation in surround pooling characteristics with RF center size results from  
constraints in the model, which maintain vSTF shape parameters that are consistent *in*  
*vivo* measurements [17] while at the same time remaining consistent with the surround  
parametric form indicated by measurements of H1 receptive fields [43]. 923  
924  
925  
926  
927  
928

Visual space-referred spatial transfer functions are commonly measured in *in vivo*  
physiological recordings that estimate spatial RF properties of mRGCs [17, 18]. The  
gray disks in Figs 7D1–7D3 depict the vSTFs of the three examined synthetic mRGCs,  
and the corresponding DoG model fits are depicted by the solid gray lines. The spatial  
RF profiles corresponding to these DoG model fits are depicted by the dashed lines in  
Figs 7C1–Figs 7C3. Contrasting these inferred spatial RF profiles with the actual cone  
pooling profiles, it becomes evident that one cannot use characterizations obtained  
under physiological optics viewing conditions to directly infer the characteristics of  
spatial pooling of cone signals in the retina. We discuss this issue further in later  
sections. 929  
930  
931  
932  
933  
934  
935  
936  
937  
938  
939

### 3.2 Validation against *in vivo* physiology across the visual field 940

To validate our model, we synthesized mRGC mosaics across a wide region of the  
retina, and computed vSTFs of individual mRGCs by probing them with drifting  
achromatic gratings of different spatial frequencies delivered to the retina under phys-  
iological optics appropriate for the eccentricity of the examined cells, simulating the  
experimental paradigm of Croner & Kaplan [17]. To compare synthetic and macaque  
mRGCs we fitted the computed synthetic cell vSTFs with the DoG model employed by  
Croner & Kaplan and compared the ratios of surround to center characteristic radii,  
 $R_s/R_c$ , and ratios of surround to center integrated sensitivities,  $K_s/K_c \times R_s^2/R_c^2$ , to  
those reported by Croner & Kaplan. 941  
942  
943  
944  
945  
946  
947  
948  
949  
950

The results of this analysis are depicted in Fig. 8, in which the left and right panels  
depict data from mRGC mosaics synthesized under the physiological optics of two  
different human observers. Figs. 8A1 and 8A2 compare macaque vs. synthetic mRGCs  
in terms of the distribution of their  $R_s/R_c$  ratios. Gray squares depict the macaque  
mRGC data and the blue density plots depict the 5%–95% percentile range of the  
 $R_s/R_c$  ratios in a population of 66,128 synthetic mRGCs. The three yellow disks in  
Fig. 8A1 correspond to the three exemplar cells illustrated in Fig. 7. Note that the  
 $R_s/R_c$  ratios in synthetic mRGCs follow the macaque data across eccentricity for  
both human subjects. The synthetic data do not, however, capture the full variance  
seen in the macaque data, as is evident by the marginal histograms (Fig. 8A3). To  
capture the full variance seen in the macaque data, we could consider synthesizing  
multiple surround pooling functions, each with different target values of  $R_s/R_c$ , and  
then randomly selecting for each synthesized mRGC from the multiple sets. 951  
952  
953  
954  
955  
956  
957  
958  
959  
960  
961  
962  
963

On the other hand, the integrated sensitivity ratios,  $K_s/K_c \times R_s^2/R_c^2$ , of the  
synthetic mRGC population, depicted in Figs. 8B1–8B3, capture both the trend with  
eccentricity and the variance of the macaque data. The variance match was achieved  
964  
965  
966

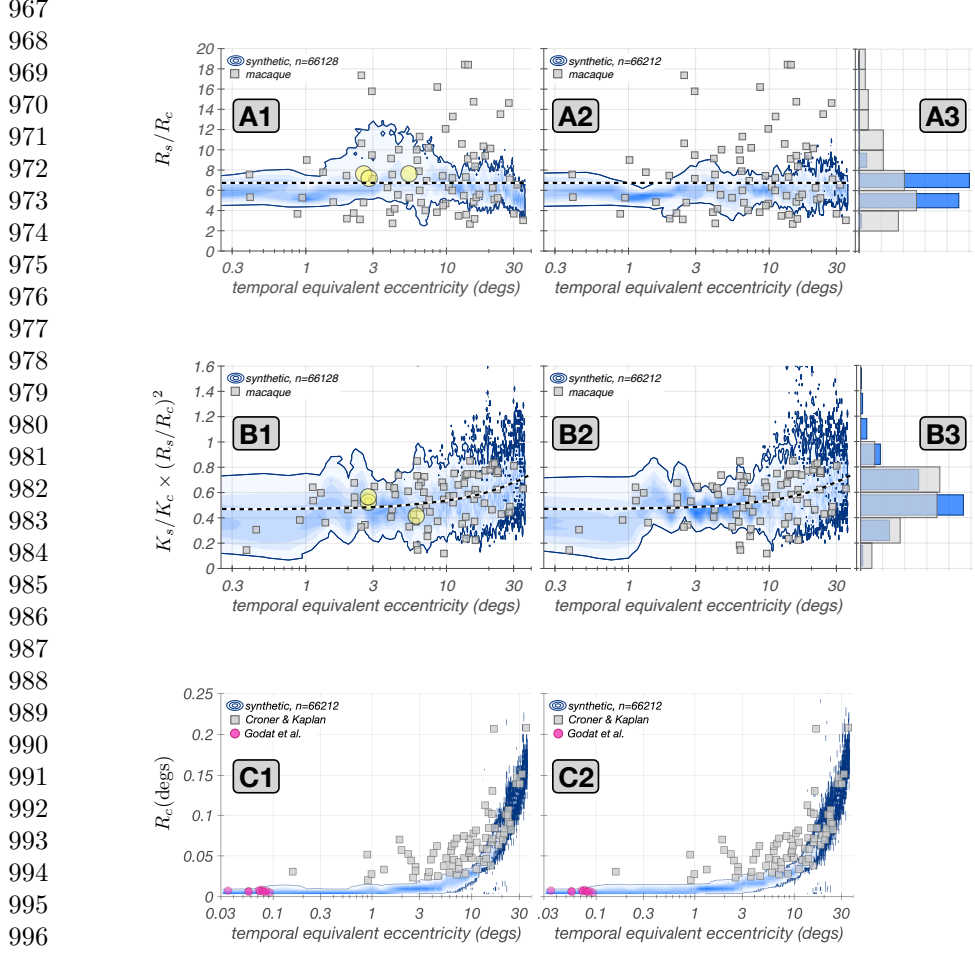


**Fig. 8 Validation against *in vivo* measurements.** In all panels, gray squares depict data from the population of macaque mRGCs recorded by Croner & Kaplan [17]. Blue contours depict the probability density function of the examined parameter in a population of 66,128 synthetic mRGCs with color saturation encoding probability level. Solid blue lines represent the 5% – 95% percentile range of examined parameter. Left and right panels are for mosaics synthesized under physiological optics of two different human subjects. **A1–A2:** Correspondence in ratio of surround-to-center characteristic radii,  $R_s/R_c$ , across eccentricity. The dashed line represents the target value that is in effect during the optimization of the synthetic mRGC surrounds, which is the mean value of  $R_s/R_c$  across the population of all mRGCs recorded by Croner & Kaplan. **A3:** Marginal histograms of  $R_s/R_c$  for macaque (gray) and synthetic mRGCs (blue). **B1–B2:** Correspondence in ratio of surround-to-center integrated sensitivities,  $K_s/K_c \times (R_s/R_c)^2$ , across eccentricity. The dashed line represents the target values in effect during the optimization of the synthetic mRGC surrounds, which is the trend observed with eccentricity in the population of the macaque mRGCs recorded by Croner & Kaplan. **B3:** Marginal histograms of  $K_s/K_c \times (R_s/R_c)^2$  for macaque (gray) and synthetic mRGCs (blue). **C1–C2:** Correspondence in RF center characteristic radius,  $R_c$ , across eccentricity. The fuschia disks represent the  $R_c$  of foveolar mRGCs recorded by Godat *et al.* [10], back-projected in visual space using the monkey's own physiological optics.

by enforcing a target variance in the  $K_s/K_c \times R_s^2/R_c^2$  ratio of the synthetic cells as described earlier.

Note that, although we did use the mean variation with eccentricity of macaque  $R_s/R_c$  and  $K_s/K_c \times R_s^2/R_c^2$  ratios during construction of the model, the model was derived using additional constraints: those imposed by the densities of cones and mRGC RFs, by the spatial characteristics of H1 horizontal cells, and by the influence of human optics. These validations, therefore, check both that we have not over constrained our model in a manner that makes it inconsistent with the macaque data, and that our method of interpolating surround pooling weights from models derived at a set of discrete retinal locations works well.

We next examined the correspondence between synthetic and macaque mRGCs in terms of their visual space-referred RF center sizes,  $R_c$ . Recall that in synthesizing mRGC mosaics, the RF centers are constructed independently of the Croner & Kaplan physiological data, using only anatomical data and estimates of RF center overlap obtained from *in vitro* physiology in the periphery [39]. Figs. 8C1–8C2 compare the distributions of  $R_c$  between the macaque and synthetic mRGCs. Note that, for both subject optics, the synthetic mRGC  $R_c$  follows the trend seen in macaque mRGCs, with good agreement at eccentricities above 10°. In more central locations, however, the  $R_c$  of the synthetic mRGCs is 2–3 times smaller than the  $R_c$  measured in macaque mRGCs. We believe that the discrepancy at central locations is not a deficiency of our model, but rather results from several factors.

First, the cone mosaic in our model has a peak density of 288,000 cones/mm<sup>2</sup> which is near the high end of densities reported in humans [36], whereas the average macaque peak cone density is around 200,000 cones/mm<sup>2</sup> [47, 51]. The higher cone density in humans implies smaller cone apertures, which in turn would bias our synthetic mRGCs towards somewhat smaller RF centers.

Second, in acute macaque experiments, the achieved optical refraction is not necessarily perfect, so there could be residual blur due to errors in refraction, as well as due to corneal edema from the contact lens used in typical multi-day acute experiments. This would increase the size of the RF centers in the physiological data relative to those in our model in central retina. Moreover, residual eye movements can occur in acute experiments, despite the ocular muscle paralysis (personal observations by N.P. Cottaris). Such residual movements would artificially enlarge estimates of RF center size for central retina mRGCs. Finally, in the macaque mRGC vSTF characterizations of Croner & Kaplan, stimulus orientation was not optimized to match any orientation bias in the RF of macaque mRGCs (Lisa Croner, personal communication), whereas in the simulated experiments, stimulus orientation was matched to the cell's visual-space referred orientation bias, which results in the smallest possible estimate of RF center size.

In additional analyses (not shown), we computed vSTFs using random grating orientations as well as a fixed orientation (as was done by Croner & Kaplan) for eccentricities between 1° and 8° along the nasal meridian. We found small effects of grating orientation on the estimates of  $R_c$  in the direction of bringing the estimated

1059  $R_c$  into closer agreement with the values reported by Croner & Kaplan. None-the-less, the enlarged estimates still fall short of the reported values, so we think the first two factors mentioned above are likely to be important.

1062 Further support for our assertion that the discrepancy in  $R_c$  between synthetic 1063 and macaque mRGCs at central locations is not a deficiency of our model, is provided 1064 by *in vivo* data from foveal macaque mRGC vSTFs obtained under adaptive optics 1065 viewing conditions [10]. The center sizes of these cells, blurred by the optics measured 1066 for the monkey subjects studied, are depicted by the purple disks in Figs. 8C1 & 8C2. 1067 Note that these align well with the  $R_c$  values of our synthetic mRGCs.

1068

### 1069 3.3 Validation against *in vitro* physiology in the periphery

1070

1071 We also compared spatial RF properties of synthetic mRGCs against macaque data 1072 from *in vitro* mRGC recordings. Since the *in vitro* data are not subject to optical blur, 1073 they may be compared directly to the retinal-space characteristics of our model. Data 1074 of this sort are currently only available in the peripheral retina.

1075 The first study considered is that of Gogliettino *et al.* [46], in which the spatial 1076 RFs of mosaics of macaque mRGCs were mapped using white noise stimulation. 1077 To simulate their experiments, we probed synthetic mRGCs with white noise modulated 1078 achromatic checkerboard stimuli delivered to the retina under diffraction limited 1079 optics. To compute the spatial RFs of synthetic mRGCs, we cross-correlated the synthetic 1080 mRGC responses with the white noise stimulus sequence. Results of this analysis 1081 are depicted in Fig. 9.

1082 In Fig. 9A the mosaics of spatial RFs in mRGC mosaics synthesized at three 1083 eccentricities, 3.5 mm, 6.75 mm and 8.5 mm, are depicted by the black ellipses. The 1084 superimposed green filled ellipses depict spatial RFs of macaque mRGCs at 3.5 mm 1085 and 8.5 mm from the study of Gogliettino *et al.*. Note that at both eccentricities, 1086 there is good correspondence in RF center size and coverage between the synthetic 1087 and the macaque mRGC mosaics. To quantify the retinal space-referred RF center 1088 sizes in synthetic mRGCs, we computed the diameter of their RF centers as  $2 \times$  1089  $\sqrt{\sigma_{\text{minor}} \times \sigma_{\text{major}}}$ , where  $\sigma_{\text{minor}}$  and  $\sigma_{\text{major}}$  are the standard deviations of the fitted 1090 Gaussian ellipsoid along its minor and major axes.

1091 The results of this analysis across eccentricity are depicted by the black dots in 1092 Fig. 9C, along with the RF center diameters of mosaics of macaque mRGCs located 1093 at 3.5 mm and 8.5 mm, which are depicted by the green squares. Note that the 1094 correspondence between synthetic and macaque data is excellent at 3.5 mm, whereas at 1095 8.5mm, the RF diameters of the synthetic mRGCs are, on average, 30–40% larger 1096 than the RF diameters of macaque mRGCs. The deviation in RF center size at the 1097 far periphery may occur because human and macaque retinas differ somewhat in the 1098 periphery. For example, in the human retina, cone density does not change much for 1099 eccentricities  $> 5\text{mm}$ , whereas in the macaque retina it continues to drop as eccentricity 1100 increases [52]. The RF size deviation we observe could be the result of a higher 1101 mRGC density in the peripheral macaque retina, relative to the human retina.

1102 The second *in vitro* study we validated our synthetic mRGCs against, is that of 1103 Field *et al.* [15], which examined the spatial layout of single cone inputs to the RF 1104 centers and surrounds in peripheral macaque mRGCs. Results of this comparison are

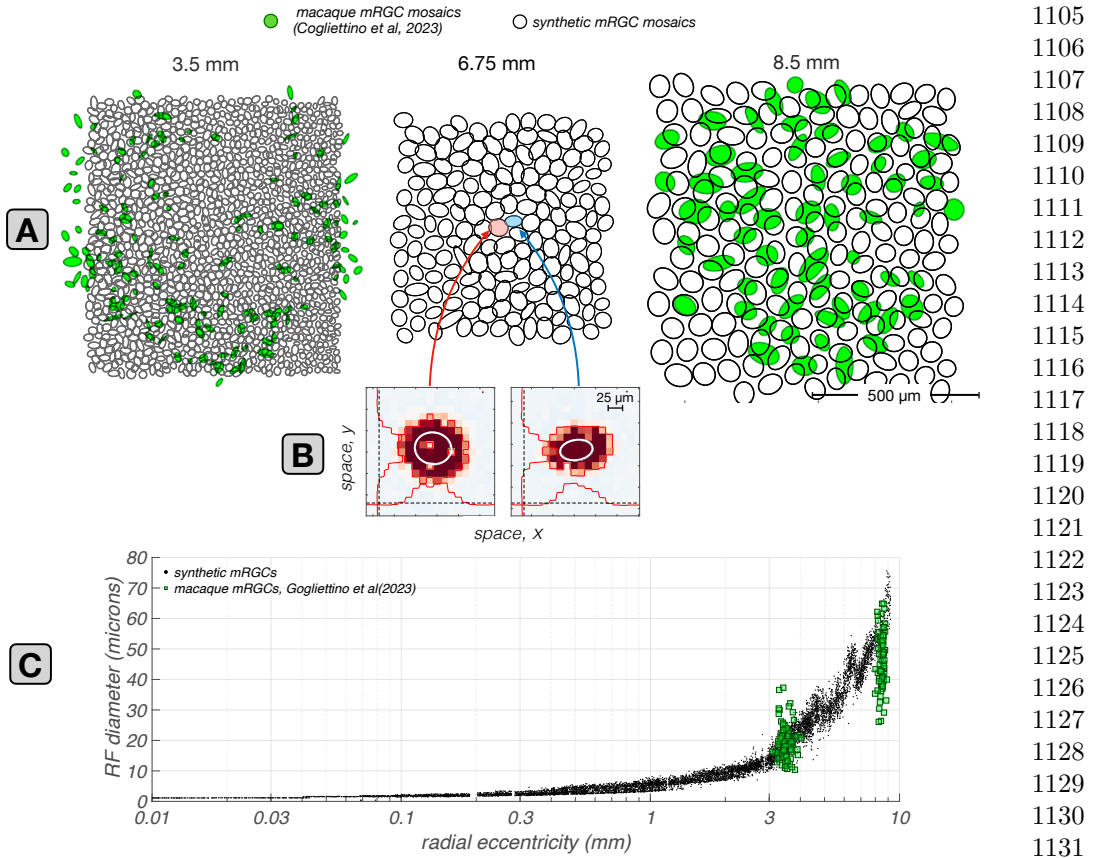
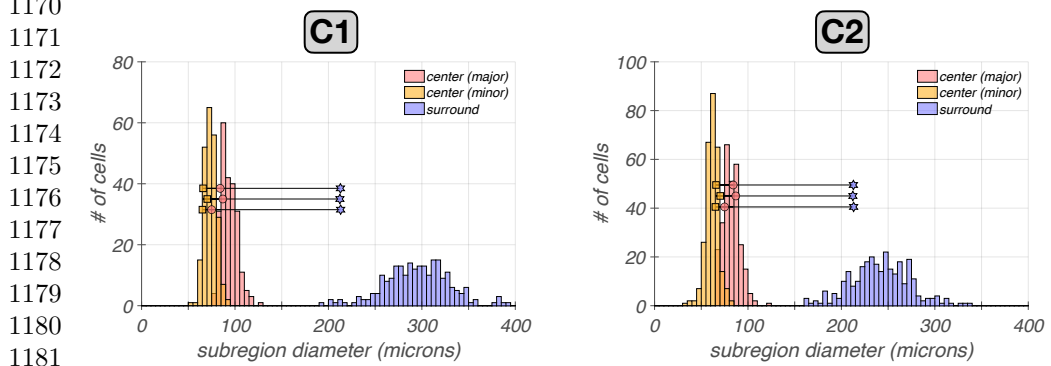
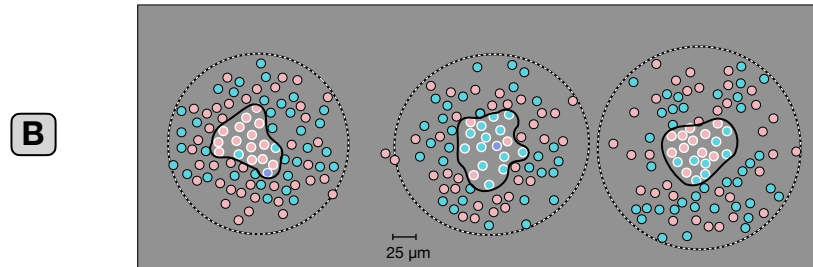
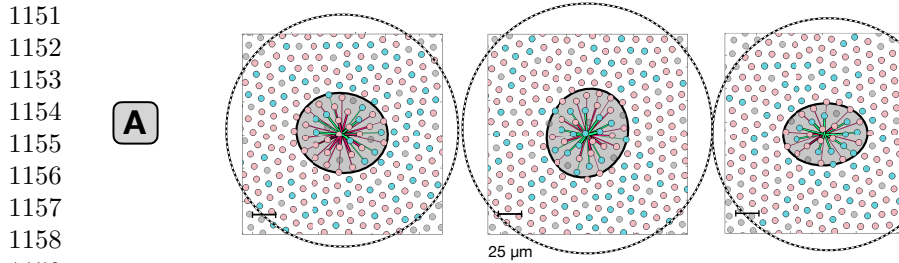


**Fig. 9 Retinal space-referred RF center sizes: synthetic vs. macaque mRGCs recorded *in vitro*.** **A:** Mosaics of synthetic mRGCs synthesized at three eccentricities, 3.5, 6.75, and 8.5 mm along the temporal meridian. The black contours depict Gaussian ellipsoid fits to the increment-excitatory regions of the computed RF maps, drawn at the  $e^{-1}$  normalized sensitivity level. Only the increment-excitatory region of the RF map is fitted. Green contours depict RF maps from two macaque mRGCs mosaics from the *in vitro* recordings of Gogliettino et al [46]. **B:** Example spatial RF maps of two synthetic mRGCs located at 6.75 mm, computed via white noise stimulation delivered to the retina under diffraction limited optics. Regions excitatory to light increments, i.e. the RF centers, and to light decrements, i.e. the RF surrounds, are indicated by red and blue colors, respectively. The scattered zero excitation spots within the light-increment RF centers correspond to the location of S-cones. White lines depict iso-contour plots of Gaussian ellipsoids fitted to the light increment-excitatory RF center region, drawn at the  $e^{-1}$  normalized sensitivity level. **C:** Comparison of synthetic against macaque mRGC RF center sizes across eccentricity. Black dots depict the RF diameters of synthetic mRGCs, computed from the Gaussian ellipsoid fits as  $2 \times \sqrt{\sigma_{\text{minor}} \times \sigma_{\text{major}}}$ , and green squares depict the RF diameters of macaque mRGCs at the two eccentricities where the *in vitro* measurements are available.

depicted in Fig. 10. Fig. 10A depicts the cone pooling maps of three synthetic mRGCs at a temporal eccentricity of 6.75 mm. The spatial distribution of cone pooling weights in three macaque mRGCs at the same eccentricity from the study of Field et al. [15], adapted from their Fig. 4, are shown in Fig. 10B. For both synthetic and macaque



1183 **Fig. 10 Cone pooling maps in RF centers and surrounds: synthetic vs. macaque mRGCs**  
1184 **recorded *in vitro*.** **A:** Center and surround cone pooling weight maps for three synthetic mRGCs  
1185 at an eccentricity of 6.75 mm along the temporal raphe. Solid and dashed contours include cones  
1186 pooled by the RF center and the RF surround, respectively, with pooling weights  $> 0.005 \times$  the peak  
1187 center weight. **B:** Center and surround cone pooling weights for three macaque mRGCs recorded in  
1188 *vitro* at an eccentricity of 6.75 mm along the temporal raphe. White and black disks indicate cones  
1189 pooled by the RF center and the RF surround respectively, with same threshold pooling weights as  
1190 in A. The macaque mRGCs are from the *in vitro* recordings of Field *et al.* [15]. **C1 &C2:** Compari-  
1191 son of minor and major diameters of the center pooling mechanism (yellow squares and pink circles)  
1192 and of the surround pooling mechanism (purple stars) in the 3 macaque mRGC cells against corre-  
1193 sponding distributions (yellow, pink and magenta histograms) in populations of synthetic mRGCs at  
1194 eccentricities of 6.75 mm (C1) and 6.0 mm (C2).

1195 mRGCs, the visualized surround cones have pooling weights  $> 0.005 \times$  the peak center  
1196 cone weight (Greg Field, personal communication).

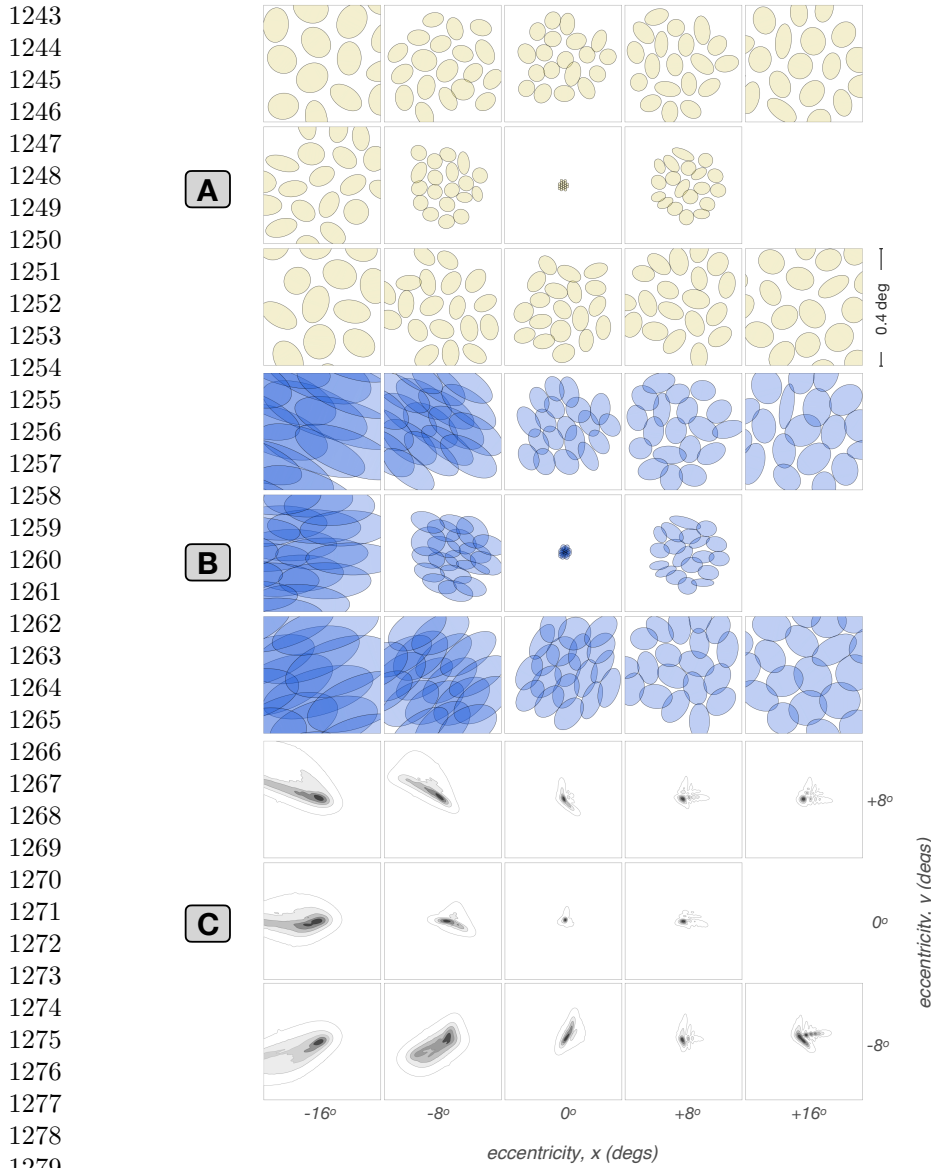
Note the general agreement between synthetic and macaque mRGCs in the extent of both their RF centers and surrounds, although again, synthetic mRGCs appear to have slightly larger RFs than their macaque counterparts. Also notable is that the density of cones in the synthetic mRGC cone pooling maps is higher than that seen in the macaque mRGCs. This occurs because our model is based on human cone mosaics, and human cone density is higher than macaque cone density at temporal eccentricities above 5 mm [52], which is where these comparisons are made.

To contrast the relationship in RF center and surround cone pooling regions between synthetic and macaque mRGCs more quantitatively, we compared the diameters of cone pooling regions of the three depicted macaque mRGCs against those of populations of synthetic mRGCs at two eccentricities: the 6.75 mm location at which the *in vitro* measurements were made, and a slightly less eccentric value of 6.0 mm. Results of this analysis are depicted in Figs. 10C1 and 10C2. The minor and major diameters of the RF center pooling mechanism and the diameter of the RF surround pooling mechanism for the 3 macaque mRGCs are depicted by the yellow squares, pink circles and magenta stars, respectively. The corresponding distributions in populations of synthetic mRGCs are depicted by the yellow, pink and magenta histograms. Note that at the 6.75 mm synthetic cell location (Fig. 10C1), the cone pooling regions of the synthetic mRGCs are larger than those of the measured macaque mRGCs. There is some uncertainty about how to best relate macaque and human retinal locations (see Methods), however, and at the slightly less peripheral eccentricity of 6.0 mm (Fig. 10C2) better agreement exists between model and macaque mRGCs. Measurements of human cone density at 6.0 mm of retina [36] are also better matched to measurements of monkey cone density at 6.75 mm [47] than are human measurements at 6.75 mm.

These observations highlight an inherent issue in building our mRGC model, namely that we had to employ a mixture of human and macaque data sources: human data regarding the density of cones and the density of mRGC RFs across visual space, human data regarding the characteristics of physiological optics across the retina, and macaque data regarding the spatial characteristics of mRGC RFs and of H1 horizontal cells, with our validations done against macaque data. This is not ideal, as there are some differences between human and macaque retinas [52]. But, it is unavoidable given the lack of complete data in either species. The modeling framework that we devised however, which incorporates data from different sources, can be easily modified as new data become available.

### 3.4 Visual *vs.* retinal space– referred RFs: the impact of physiological optics

In this section we characterize how physiological optics interacts with the retinal cone pooling within the RFs of mRGCs to shape their visual space–referred RF properties. Fig. 11 illustrates examples of this interaction at five horizontal eccentricities,  $x = [-16^\circ, -8^\circ, 0^\circ, +8^\circ, +16^\circ]$ , and 3 vertical eccentricities,  $y = [-8^\circ, 0^\circ, +8^\circ]$ . The yellow ellipses in each panel of the  $3 \times 5$  grid of Fig. 11A depict Gaussian ellipsoids fitted to the retinal space–referred RF maps of synthetic mRGCs at the examined eccentricities. The small and non-systematic orientation biases in the retinal space–referred RF maps



1280 **Fig. 11 Retinal vs. visual space-referred mRGC RF maps across the retina.** Illustration  
 1281 of the effect of physiological optics on visual space-referred spatial RF maps of synthetic mRGCs  
 1282 across eccentricity. **A:** Retinal space-referred spatial RF maps at different ( $x,y$ ) eccentricities. Within  
 1283 each panel, yellow contours depict Gaussian ellipsoid fits to RF maps of up to 19 cells from a single  
 1284 mRGC mosaic. RF maps are computed using white noise stimulation under diffraction limited optics.  
 1285 **B:** Visual space-referred spatial RF maps of the same cells, computed under physiological optics  
 1286 of one human subject at corresponding eccentricities. **C:** Point spread functions of the employed  
 1287 physiological optics at corresponding eccentricities.  
 1288

emerge due to the pooling of multiple cones by the RF center mechanism and are reminiscent of RGC mosaics mapped *in vitro* [39]. 1289  
1290

The blue ellipses in Fig. 11B depict Gaussian ellipses fitted to the visual space-referred RF maps of the same cells. Note that there are striking and systematic orientation biases in these visual space-referred RF maps, which emerge due to the characteristics of physiological optics, whose PSFs are depicted in Fig. 11C. Clearly, the shape of the PSFs, especially at peripheral locations is a major determinant of the visual space-referred RFs in mRGCs. 1291  
1292  
1293  
1294  
1295  
1296

Overall, this analysis demonstrates that there can be substantial differences between *in vivo* and *in vitro* estimates of the spatial RFs of mRGCs, and, once again highlights the notion that inferences regarding retinal wiring from *in vivo* measurements must be evaluated in the context of the effect of the physiological optics. Indeed, in recent on-going work, [32], we have shown the importance of such analyses in assessing inferences regarding cone wiring to the surround subregions of mRGCs based on *in vivo* measurements of their spatio-chromatic RFs. 1297  
1298  
1299  
1300  
1301  
1302  
1303  
1304

### 3.5 Validity of the Difference of Gaussians model applied to *in vitro* responses of mRGCs in retrieving their spatial pooling characteristics 1305 1306 1307 1308

In our synthetic mRGCs, the spatial characteristics of cone pooling within the RF center and the RF surround *component* mechanisms are known by design. This allows us to test how well one can predict these characteristics from DoG model fits to *in vitro* measurements of mRGC STFs, where the RF center and surround mechanisms are driven simultaneously in the absence of optics [16]. 1309  
1310  
1311  
1312  
1313

Results of this analysis are illustrated in Fig. 12. The cone pooling maps of four exemplar mRGCs are depicted in the left column. The cells in the top two rows both have RF centers with a single cone input, whereas the cell in the third row has a 2-cone RF center, and the cell in the fourth row has a 3-cone RF center. The pink and maroon histograms depicted in the middle column of Fig. 12, are the y-axis integrated cone pooling weights within these cells' RF center and surround subregions, respectively. The superimposed dashed lines depict the center and surround line weighting profiles, as estimated by the DoG model fit to the cells' retinal space-referred STFs, which are depicted by the gray disks in the right column of Fig. 12. 1314  
1315  
1316  
1317  
1318  
1319  
1320  
1321  
1322

Note that although the DoG model fits to the computed retinal space-referred STFs (solid lines in right column) are good for all cells, the inferred spatial RF profiles, (dashed lines in the middle column) do not capture accurately the cone pooling regions of the RF surrounds (slate histograms in the middle column). The discrepancy between actual and inferred surround pooling is most obvious in the two top cells which have single-cone RF centers, and becomes less pronounced as RF center size increases. The discrepancy involves both the spatial extent and the peak sensitivity of the inferred surround pooling, which is estimated by the DoG model to be more diffuse with a weaker peak sensitivity than the cell's actual surround cone pooling. 1323  
1324  
1325  
1326  
1327  
1328  
1329  
1330  
1331

It is perhaps not surprising that the DoG model does not do a good job of fitting the model cell surrounds, given that they were constructed as double exponentials to match the spatial properties of H1 horizontal cells. The key point, however, is that the 1332  
1333  
1334

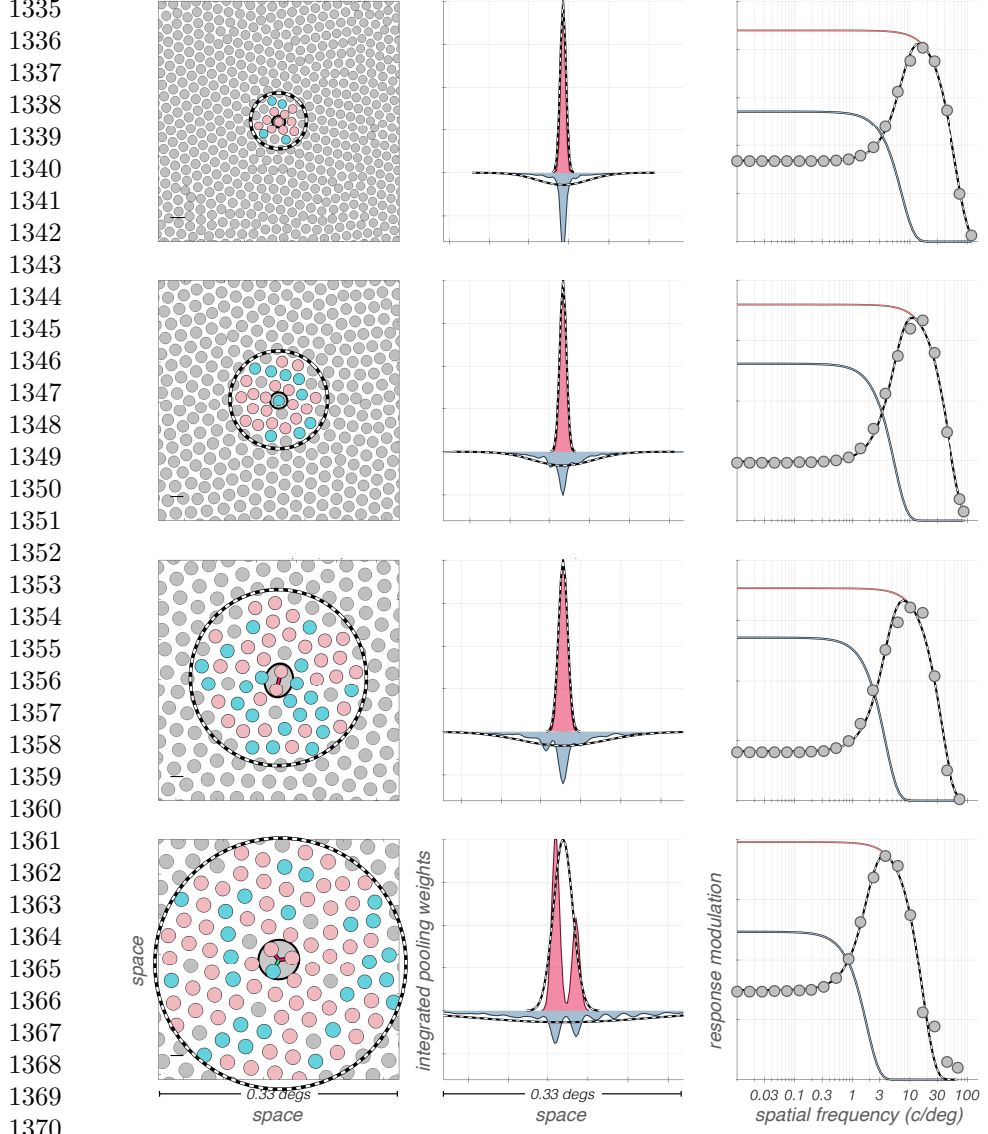


Fig. 12 Spatial characteristics of mRGC surround cone pooling inferred from DoG model fits to retinal space-referred vSTFs are not accurate. The correspondence between actual and inferred surround cone pooling is examined for exemplar synthetic mRGCs at four eccentricities. **Left panels:** Cone input maps of RF center and RF surround mechanisms. **Middle panels:** Line weighting functions of cone inputs pooled by the RF center and the RF surround mechanisms, depicted by pink and slate histograms, respectively. Dashed lines represent line weighting functions as inferred from DoG model fits to the cells' retinal space-referred STFs. **Right panels:** Retinal space-referred STFs, depicted by gray disks, computed for stimuli delivered to the retina via diffraction limited optics. The DoG model fits to the computed STFs are depicted by the dashed black lines, with the corresponding center and surround components depicted by the pink and slate lines, respectively.

DoG model fits to the observable composite STFs are quite good. These observations suggest that caution should be exercised when inferring mRGC RF surround properties from DoG model fits to <i>in vitro</i> STF measurements.	1381
	1382
	1383
	1384
	1385
	1386
	1387
	1388
	1389
	1390
	1391
	1392
	1393
	1394
	1395
	1396
	1397
	1398
	1399
	1400
	1401
	1402
	1403
	1404
	1405
	1406
	1407
	1408
	1409
	1410
	1411
	1412
	1413
	1414
	1415
	1416
	1417
	1418
	1419
	1420
	1421
	1422
	1423
	1424
	1425
	1426

1427 with templates provided by the noise-free mRGC responses to the stimuli being dis-  
1428 criminated. For comparing computational observer performance at the mRGCs with  
1429 that at the cones, we also adopted the Gaussian noise approximation for the cone  
1430 excitations, and used the template matching decision rule.

1431 To estimate contrast sensitivity, we varied, for each tested spatial frequency,  $\omega$ ,  
1432 the contrast of the test stimulus and identified threshold contrast,  $C_{\text{threshold}}(\omega)$ , as  
1433 that for which the probability of correctly identifying the test versus a zero contrast  
1434 stimulus was 80.6%. Contrast sensitivity was defined as  $\text{CSF}(\omega) = 1/C_{\text{threshold}}(\omega)$ .

1435 Estimates of so computed contrast sensitivities at three eccentricities are depicted  
1436 in Fig. 13. The contrast sensitivities for stimuli viewed through typical human optics  
1437 are shown in the left panels of Fig. 13, with disks and triangles depicting sensitivity  
1438 at the mRGC mosaic and at its input cone mosaic, respectively. For comparison,  
1439 the right panels of Fig. 13 depict corresponding calculations for stimuli viewed under  
1440 diffraction-limited optics with no chromatic aberration, as might be measured using  
1441 adaptive optics. The comparison between left and right panels helps understand which  
1442 effects in the computed CSFs have their origin in the optics or sampling by the cone  
1443 mosaic, and which should be attributed to retinal processing through to the mRGCs.

1444 At the fovea, the CSFs at the cone excitation level (triangles in Fig. 13A1), are  
1445 low pass for both achromatic and L – M stimuli. This is expected because there is no  
1446 spatial antagonism at the level of the photopigment excitations, and because we do  
1447 not incorporate spatio-temporal coupling that arises because of interactions between  
1448 fixational eye movements and post-receptor temporal filtering [56, 57].

1449 On the other hand, the achromatic CSF at the mRGC mosaic exhibits a mild low-  
1450 spatial frequency attenuation, which is due to the spatial antagonism between the RF  
1451 centers and surrounds. Note that the low frequency attenuation appears weaker than  
1452 what is observed under diffraction limited optics (Fig. 13A2). This occurs because  
1453 physiological optical blur carves sensitivity at the high frequency regime, thereby  
1454 reducing the apparent effect of the mRGC surrounds on the CSF. We observed a sim-  
1455 ilar effect in foveal macaque mRGCs whose responses were measured under adaptive  
1456 optics conditions [10].

1457 The L – M opponent CSF of the mRGC mosaic lacks the low-frequency attenuation  
1458 seen for achromatic modulations because in foveal mRGCs, L – M cone opponent  
1459 stimuli do not induce substantial spatial antagonism between their single cone RF  
1460 centers and their surrounds. These observations, which are consistent with what is  
1461 known regarding the L – M chromatic contrast sensitivity of the mRGC pathway  
1462 [16, 58], demonstrate that L – M sensitivity exceeds achromatic sensitivity at low  
1463 spatial frequencies, consistent with the literature [59].

1464 At high spatial frequencies there is little difference between computational observer  
1465 sensitivity to achromatic and L – M modulations. This is not true of human observers,  
1466 where sensitivity drops more rapidly as a function of spatial frequency for red-green  
1467 isoluminant gratings than for achromatic gratings, either with [58] or without typical  
1468 optical blur [60]. Although our L – M opponent CSFs are not precisely equivalent to  
1469 the red-green isoluminant CSFs measured in many human experiments, this is not  
1470 the primary source of the difference between computational and human observers.  
1471 Rather, it is known that compared to ideal observers, humans lose foveal information  
1472

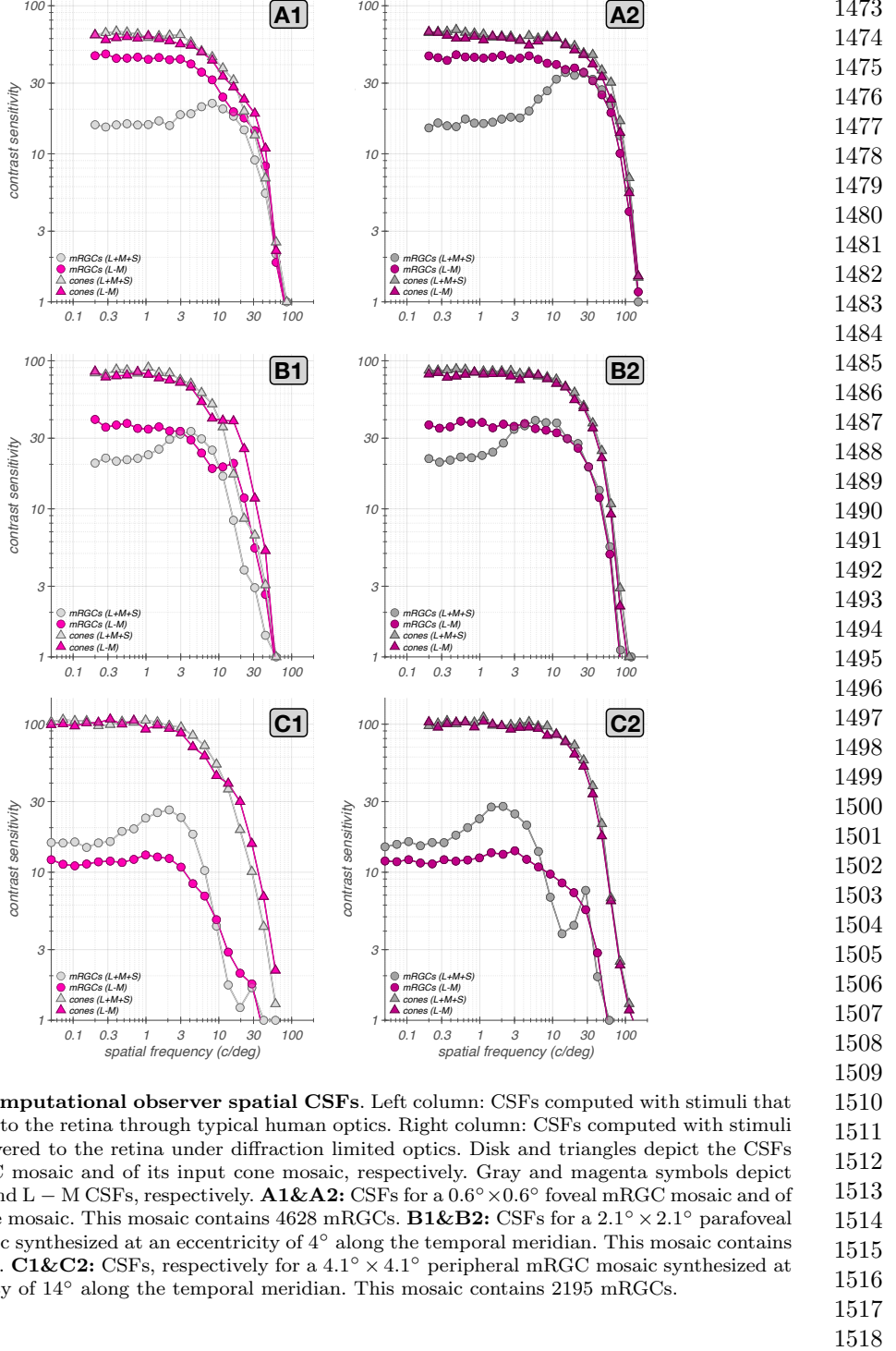


**Fig. 13 Computational observer spatial CSFs.** Left column: CSFs computed with stimuli that are delivered to the retina through typical human optics. Right column: CSFs computed with stimuli that are delivered to the retina under diffraction limited optics. Disk and triangles depict the CSFs of the mRGC mosaic and of its input cone mosaic, respectively. Gray and magenta symbols depict achromatic and L – M CSFs, respectively. **A1&A2:** CSFs for a  $0.6^\circ \times 0.6^\circ$  foveal mRGC mosaic and of its input cone mosaic. This mosaic contains 4628 mRGCs. **B1&B2:** CSFs for a  $2.1^\circ \times 2.1^\circ$  parafoveal mRGC mosaic synthesized at an eccentricity of  $4^\circ$  along the temporal meridian. This mosaic contains 4633 mRGCs. **C1&C2:** CSFs, respectively for a  $4.1^\circ \times 4.1^\circ$  peripheral mRGC mosaic synthesized at an eccentricity of  $14^\circ$  along the temporal meridian. This mosaic contains 2195 mRGCs.

1519 available from the cones more rapidly as a function of spatial frequency for red-green  
1520 than than for achromatic gratings [55]. Our example calculation here suggests that this  
1521 information loss should not be attributed to the linear receptive fields of the mRGCs.

1522 We believe this is because optical blur dominates computational observer perfor-  
1523 mance at high spatial frequencies and the single cone RF centers of foveal mRGCs  
1524 transmit information about each type of stimulus equally well; the surrounds have lit-  
1525 tle effect at high spatial frequencies. Also, we do note that, in the present calculations,  
1526 the specific resolution limit, i.e., the spatial frequency at which sensitivity drops to  
1527 1, depends on the variance of the added Gaussian noise and is thus somewhat arbit-  
1528 trary. We have chosen a noise level that is low relative to human observers so that our  
1529 computations show the behavior in the high-spatial frequency regime more fully than  
1530 would psychophysics conducted through natural optics.

1531 As we move to more peripheral locations, additional features of the CSF emerge.  
1532 Figs. 13B1 and 13C1 depict results of computations at 4° along the temporal meridian.  
1533 Note that under physiological optics viewing (Fig. 13B1) there is a spatial frequency  
1534 regime in which L – M sensitivity exceeds the corresponding achromatic sensitivity,  
1535 with the L – M CSF having a notched shape. We have reported this observation in  
1536 conference abstract form [61]. It occurs because of the wavelength dependent defocus  
1537 that is introduced by longitudinal chromatic aberration (LCA), which can change  
1538 the spatial phase of the L– and M-cone stimulus components in the retinal image.  
1539 Consistent with this interpretation, the notch is present in the CSFs both at the cones  
1540 and at the mRGCs on the left, but not under diffraction-limited optics (Fig. 13B2),  
1541 where LCA is zero. Similar effects have been observed for S-cone CSFs [62]. We have  
1542 presented in abstract form experimental results that suggest that these effects occur  
1543 in measurements of the human L – M spatial CSF [63].

1544 Comparison of the cone-based CSFs in Fig. 13A1 with those in Fig. 13B1 and  
1545 Fig. 13C1 reveals the effect of stronger optical blur with eccentricity, which increases  
1546 the rolloff of the CSFs with spatial frequency. Similar comparison of the mRGC-based  
1547 CSFs shows additional rolloff introduced by the increasing size of mRGC RF centers  
1548 with eccentricity.

1549 Additional observations are notable at 14° (Figs. 13C1 and 13C2). First, a notch  
1550 arises in the achromatic CSF at high spatial frequencies for the mRGC CSF that is  
1551 not apparent in the cone CSF. This seems unlikely to be an optical effect, because it  
1552 is more salient in Fig. 13C2 where optical effects are not present. To explore the origin  
1553 of this effect, we computed CSFs at different orientations (not shown), which show  
1554 that this notch is orientation dependent and has to do with the precise alignment of  
1555 individual cones with the receptive field of an mRGC. We do not explore it further  
1556 here.

1557 We note that our computational observer is with respect to an RGC noise level  
1558 that may make it more sensitive than the human observer. If so, the notches shown  
1559 in Fig. 13 might not be revealed with psychophysics. In further simulations (data  
1560 not shown) conducted with twice the noise variance, we observed that, in addition to  
1561 an overall reduction in sensitivity, the high frequency notches disappeared below the  
1562 sensitivity floor. Therefore, the effects shown in Fig. 13, if they exist, are most likely  
1563 to be revealed under conditions that maximize psychophysical sensitivity (i.e., bright  
1564

adapting background, stimuli that fill the spatial and temporal integration area and duration, adaptive optics viewing). 1565  
1566

Finally, note that the L – M advantage over the achromatic CSF is reversed at 14° of eccentricity. This is because at such high eccentricities, the L – M signal is reduced by the increased mixing of L– and M–cone signals within the larger mRGC RF centers and surrounds. Careful comparison of this effect with computational observer predictions for various choices of the model’s spatial homogeneity/spectral purity tradeoff parameter,  $\phi$ , is an interesting future direction. 1567  
1568  
1569  
1570  
1571  
1572  
1573

### 3.6.2 Chromatic contrast sensitivity of synthetic mRGC mosaics: dependence on eccentricity 1574 1575 1576

As a second example application, we examined chromatic sensitivity for uniform fields modulated along different directions in the L/M–cone contrast plane. We used the same computational observer approach described above, and evaluated threshold for stimuli whose contrast was modulated in time. The cone contrasts of stimuli at different chromatic directions,  $\theta$ , on the LM plane were:  $C_L(\theta) = \rho \cdot \cos(\theta)$ ;  $C_M(\theta) = \rho \cdot \sin(\theta)$ ;  $C_S(\theta) = 0$ . For each  $\theta$ , we varied  $\rho$  to find its threshold value for discriminating that modulation direction from a zero contrast stimulus with a probability of 80.6%. To summarize the computed thresholds across the different chromatic directions, we fit ellipses to the locus of threshold contrast points. 1577  
1578  
1579  
1580  
1581  
1582  
1583  
1584  
1585  
1586  
1587  
1588  
1589  
1590  
1591  
1592  
1593  
1594  
1595  
1596  
1597  
1598  
1599  
1600  
1601  
1602  
1603  
1604  
1605  
1606  
1607  
1608  
1609  
1610

Fig. 14 depicts computational observer thresholds for synthetic mRGC mosaics and for their input cone mosaics at different eccentricities. Note that how computational observer sensitivity changes with eccentricity depends on how stimulus size is covaried with eccentricity, as does human sensitivity (e.g. [64]). Comparison of the magnitude of sensitivity for cone– and mRGC–based computational observers depends on how the noise levels are chosen. For these example calculations, we focus on the shape rather than magnitude of the elliptical threshold contours. Therefore, each contour shown in Fig. 14 is normalized so that the threshold along the M cone direction is equal to one.

A few observations are notable. First, the normalized contours for the cone mosaic–based observer are similar across eccentricities and align with the L– and M–cone contrast axes. They are more elongated in the M–cone direction because our mosaics have more L cones than M cones. The alignment with the axes is expected [65], and the similarity of the normalized shapes occurs because this shape depends primarily on the relative numbers of L and M cones. 1594  
1595  
1596  
1597  
1598  
1599  
1600  
1601  
1602  
1603  
1604  
1605  
1606  
1607  
1608  
1609  
1610

Second, in contrast to the cone mosaic–based thresholds, the mRGC mosaic–based threshold contours change markedly with eccentricity. For the foveal mRGC mosaic, the threshold ellipse is highly elongated along 45° in the L/M–cone contrast plane, indicating that the highest discrimination thresholds occur when  $C_L = C_M$  and lowest thresholds occur when  $C_L = -C_M$ . This difference in comparison to the cone–based computations is a consequence of the chromatic–opponency of foveal mRGC RFs, which have single cone centers, and thus opponency between their centers and the surrounds as the surrounds draw on mixed cone-types [66, 67]. This opponency leads to cancellation of non–opponent L– and M–cone signals for low spatial frequency stimuli and thus the observed contour elongation along 45° [65, 68].

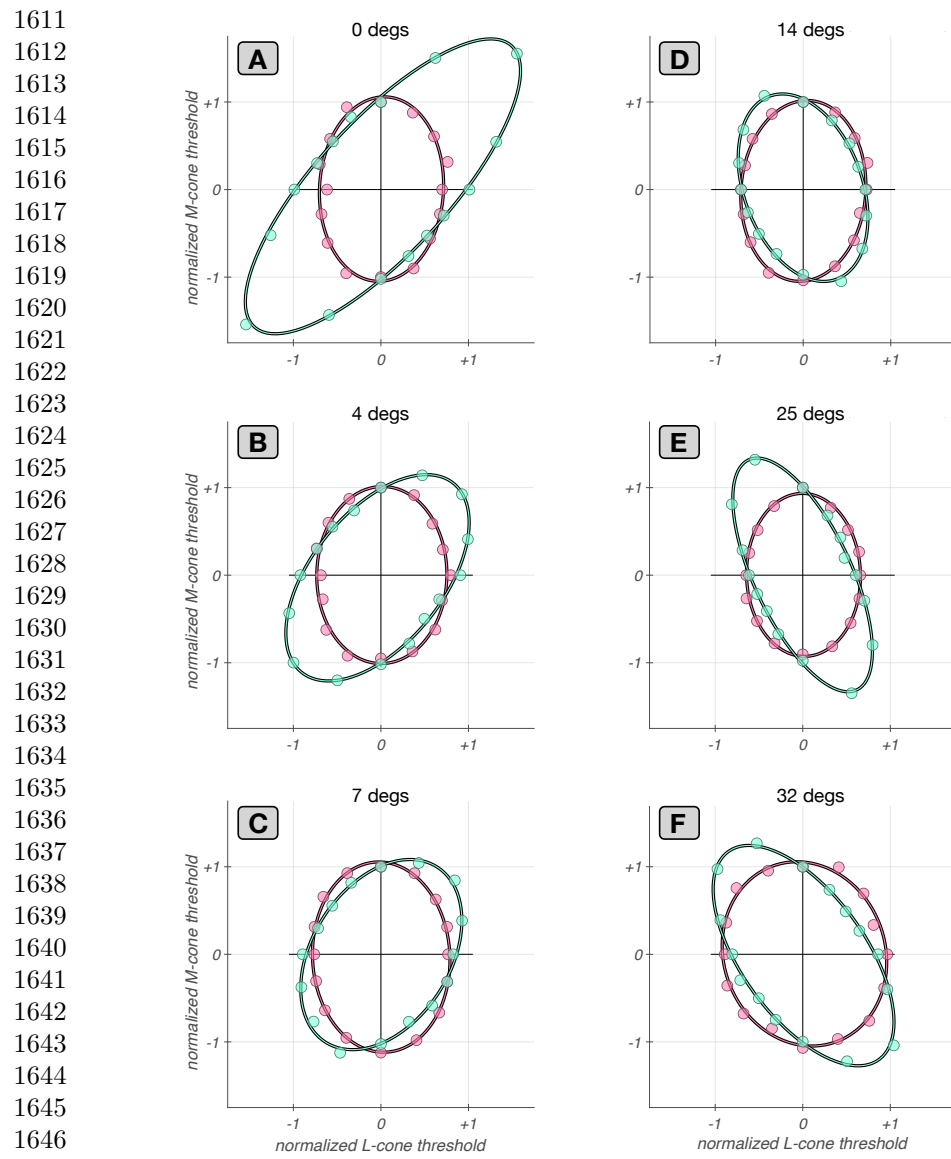


**Fig. 14 Chromatic contrast sensitivity of synthetic mRGC mosaics: dependence on eccentricity.** Discrimination thresholds along the L/M-cone contrast plane of mRGC mosaics (green disks) and of their input cone mosaics (pink disks), computed for uniform field stimuli (0 c/deg). **A:** Data from a  $0.6^\circ \times 0.6^\circ$  foveal mRGC mosaic. **B:** Data from a  $2.1^\circ \times 2.1^\circ$  parafoveal mRGC mosaic synthesized at an eccentricity of  $4^\circ$  along the temporal meridian. **C:** Data from a  $3.2^\circ \times 3.2^\circ$  parafoveal mRGC mosaic synthesized at an eccentricity of  $7^\circ$  along the temporal meridian. **D:** Data from a  $4.1^\circ \times 4.1^\circ$  peripheral mRGC mosaic synthesized at an eccentricity of  $14^\circ$  along the temporal meridian. **E:** Data from a  $6^\circ \times 6^\circ$  peripheral mRGC mosaic synthesized at an eccentricity of  $25^\circ$  along the temporal meridian. **F:** Data from a  $9^\circ \times 9^\circ$  peripheral mRGC mosaic synthesized at an eccentricity of  $32^\circ$  along the temporal meridian.

Third, as eccentricity increases, the contours first become less elongated and then elongation starts increasing again but along the 135° rather than the 45° axis. This is because the cone non-selective wiring model we implemented leads to progressively less opponency with increasing RF center size [16, 66, 67].	1657
	1658
	1659
	1660
	1661
	1662
	1663
	1664
	1665
	1666
	1667
	1668
	1669
	1670
	1671
	1672
	1673
	1674
	1675
	1676
	1677
	1678
	1679
	1680
	1681
	1682
	1683
	1684
	1685
	1686
	1687
	1688
	1689
	1690
	1691
	1692
	1693
	1694
	1695
	1696
	1697
	1698
	1699
	1700
	1701
	1702

1703 approach of fitting a Difference of Gaussian model to spatial responses can lead to  
1704 incorrect assessments of the properties of cone pooling in the mRGC surrounds.

1705

#### 1706 4.1 Applications

1707

1708 We employed an early version of the current model to interpret measurements of  
1709 foveal macaque mRGCs measured *in-vivo* using adaptive optics [10]. Specifically, the  
1710 model allowed us to relate the adaptive optics measurements to *in-vivo* measurements  
1711 conducted under physiological optics. For this purpose, the ability to move back and  
1712 forth between retinal and visual space-referred representations was critical.  
1713

1714 We are currently employing the model to assess inferences regarding the wiring of  
1715 cone inputs to mRGC RF surrounds based on spatial RF measurements conducted *in-*  
1716 *vivo* [19]. Specifically, we are analyzing the substantial effect that chromatic aberration  
1717 plays in shaping mRGC responses to cone isolating stimuli, and how these effects can  
1718 help reconcile tension between results from *in-vivo* physiology on the one hand and  
1719 results from anatomy and *in-vitro* physiology on the other [32].

1720 In parallel on-going work, we deploy the model to understand how the spatio-  
1721 chromatic properties of the ON-center mRGC mosaic influence the information  
1722 available for human spatio-chromatic vision, by applying computational observer anal-  
1723 yses to the mRGC representation we compute [61, 63]. Although additional model  
1724 components will influence this representation, for threshold tasks, where the stimulus  
1725 perturbations are small, we expect the linear approximation to hold sufficiently well  
1726 that the results will be informative.

1727 In this work, we presented examples of this type of computation, to illustrate how  
1728 the representation at the mRGCs differs from that at the cone mosaic and how this  
1729 varies with eccentricity.

1730

#### 1731 4.2 Limitations and Future Directions

1732

1733 We conclude with discussing the various limitations of the model in its present state  
1734 and our plans for augmenting the model to increase its realism.

1735

##### 1736 4.2.1 Human versus macaque

1737

1738 When available, we used human data to guide model development, in order to maxi-  
1739 mize the usefulness of the model in predicting human performance. Even if this had  
1740 not been our goal, we would have had to bring in human data to characterize the  
1741 physiological optics across the visual field, as such data are not currently available in  
1742 macaque. At the same time, not all the required data are available for human: although  
1743 measurements of cone and mRGC density and physiological optics across the retina  
1744 are available, physiological characterizations come from the macaque.

1745 The need to mix data across the two closely related species produces tension in  
1746 cases where the parameters for the two species differ. An example is the different  
1747 cone densities in the far periphery [52], which intrudes on the interpretation of the  
1748 comparison between our model and *in-vitro* physiology in that retinal region. As more  
1749 data become available in both species, and as species differences come more fully into  
1750

focus [69], our approach should allow more fully differentiated models to be developed targeted at each. 1749  
1750

#### 4.2.2 Noise, nonlinearities and temporal dynamics 1751

Although the current model captures fundamental aspects of the visual representation at the level of the mosaic of ON–center mRGCs, there are known characteristics of mRGCs that it does not account for. These include static and spatial nonlinearities, temporal filtering, spike generation, and physiologically constrained response noise. The modeling framework we developed is extensible however, so that these components may be included through future work. 1752  
1753  
1754  
1755  
1756  
1757  
1758  
1759  
1760  
1761  
1762  
1763  
1764  
1765  
1766  
1767  
1768  
1769  
1770  
1771  
1772  
1773  
1774  
1775  
1776  
1777  
1778  
1779  
1780  
1781  
1782  
1783  
1784  
1785  
1786  
1787  
1788  
1789  
1790  
1791  
1792  
1793  
1794

Response variability models are available for macaque mRGCs, as descriptions of spike generation mechanisms [26, 28, 70]. In addition, we can incorporate nonlinearities, such as (a) light adaptation effects introduced through the phototransduction cascade [71], (b) compressive and expansive static nonlinearities in the output of mRGCs [23, 28], and (c) spatial nonlinearities introduced by rectifying sub-units within the RFs of mRGCs [21, 22]. Explicit inclusion of photocurrent-based responses in the input to the mRGCs introduces a temporal component to the response model [71]. In addition, a second temporal filter may be added, such that when combined with the photocurrent filter will yield the bandpass filter characteristics observed in macaque mRGCs [25].

Our current model does not represent explicitly the properties of the retinal circuitry (horizontal, bipolar, and amacrine cells) that produces the mRGC response properties, as we have opted instead to work towards a functional model that describes those properties. A complementary mRGC modeling approach that does consider some of these cell types explicitly has recently been published [31], and there are other modeling efforts that have examined the influence of the various retinal interneurons on RGC response properties [29, 33]. We note however, that some of the processing performed by these other retinal cell types is incorporated implicitly in the current cone-to-mRGC model, such as the parametric form of the surrounds inherited from H1 cells.

The framework we developed is designed so that it would be possible to interpose explicit models of intermediate retinal cell types. Representing the action of different cell types explicitly may in the longer run be an effective way to account for response nonlinearities in the mRGCs, or in other classes of retinal ganglion cells. Moreover, using our framework to model other cell classes may be of interest to those seeking to interpret responses of those classes *per se*, or in the retinal mechanisms that produce RGC response properties.

#### 4.2.3 OFF mRGC mosaic 1787

Because we model the linear RF, the distinction between ON and OFF mRGCs is subtle. However, our model should be thought of as a model of only the ON–center mRGCs because the synthetic cells only pool signals from L– and M–cones. This is believed true for ON–center mRGCs, but recent evidence suggests that OFF–center mRGCs draw upon all three types of cones in their RF centers [15, 37, 38]. Incorporating S-cone input into an OFF–center mRGC model is straightforward. 1788  
1789  
1790  
1791  
1792  
1793  
1794

1795 Another question that arises when considering a model of the OFF-center mRGC  
1796 mosaic is how to split the density of mRGCs in two populations at different eccentric-  
1797 ities. In the current model, the density of ON-center mRGCs was assumed to be half  
1798 of the total mRGC density across all eccentricities. This seems reasonable for central  
1799 retina where mRGC centers draw primarily on a single cone and where anatomical evi-  
1800 dence suggests that each cone provides input to the center of one ON-center and one  
1801 OFF-center midget bipolar cell. However, there is evidence that the RFs of peripheral  
1802 ON-center midget (and parasol) RGCs are larger than their OFF-center counterparts  
1803 in both human and macaque retinas [40]. This implies that the density of ON-center  
1804 RGC cells might be lower in the periphery than that of OFF-center cells, given that  
1805 ON- and OFF-center mRGCs have similar RF overlap [39]. One idea is to treat this  
1806 asymmetry in mRGC density in an eccentricity-dependent manner, similar to the way  
1807 we encoded a variable-with-eccentricity RF center overlap.

1808 Finally, when adding an OFF-center mRGC mosaic, one should allow for the  
1809 possibility of coordination between the ON- and the OFF-center mosaics, to account  
1810 for recent observations regarding systematic shifts in the spatial layouts of ON- and  
1811 OFF-center mRGCs [72].

1812

### 1813 **Using the software**

1814

1815 The developed software for synthesizing ON-center mRGC mosaics across the retina  
1816 and for computing with them is part of ISETbio and is freely available at  
1817 <https://github.com/isetbio/isetbio>. An introduction to using the mRGCmosaic  
1818 software is available at:

1819 [https://github.com/isetbio/isetbio/wiki/Retinal-ganglion-cell-\(RGC\)-mosaics](https://github.com/isetbio/isetbio/wiki/Retinal-ganglion-cell-(RGC)-mosaics).

1820 A number of MATLAB tutorials specific to the ON-center mRGCmosaic can be  
1821 found at <https://github.com/isetbio/isetbio/tree/main/tutorials/mrgc>.

1822 These tutorials demonstrate (a) how to use mosaics of ON-center mRGCs that  
1823 we have already synthesized at a number of eccentricities, and (b) how to build and  
1824 validate ON-center mRGC mosaics at any desired eccentricity, using a number of  
1825 design choices. A summary of current available tutorials is shown in Table 1.

1826 **Acknowledgements.** We thank Lisa Croner and the late Ehud Kaplan for help  
1827 with procedures followed during collection of the macaque *in vivo* data, Greg Field for  
1828 providing insight on details regarding *in vitro* macaque data, and E. J. Chichilnisky,  
1829 Tyler Godat, David Williams, and Fangfang Hong for helpful discussions.

1830

### 1831 **Declarations**

1832

### 1833 **Funding**

1834

1835 This work was supported by Facebook Reality Labs and by the Air Force Office of  
1836 Scientific Research (FA-9550-22-1-0167 and FA-9550-22-1-0044).

1837

### 1838 **Conflict of interest/Competing interests**

1839

1840 Not applicable

**Table 1** List of tutorials for computing with existing mRGC mosaics and for *de novo* synthesis of mRGC mosaics.

Tutorial name	Scope	
<i>Computing with mRGC mosaics</i>		
<code>t_mRGCMosaicVisualizeWithOptics.m</code>	Visualizes a previously synthesized mRGC mosaic and the optics that were used for its synthesis	1841 1842
<code>t_mRGCMosaicInspect.m</code>	Visualizes an mRGCMosaic and cone pooling maps of individual cells	1843 1844 1845
<code>t_mRGCMosaicBasicComputation.m</code>	Perform a basic computation with an mRGC mosaic	1846 1847 1848
<i>Synthesizing mRGC mosaics</i>		
<code>t_mRGCMosaicSynthesizeAtStage1.m</code>	Denovo synthesis of the spatial position lattices of cones and mRGC RF centers (stage 1)	1849 1850 1851 1852 1853
<code>t_mRGCMosaicSynthesizeAtStage2.m</code>	Denovo synthesis of an mRGC mosaic at different sub-stages of cone-to-mRGC RF center connectivity (stage 2)	1854 1855 1856 1857
<code>t_mRGCMosaicSynthesizeAtStage3.m</code>	Denovo synthesis of an mRGC mosaic at different sub-stages of cone-to-mRGC RF surround connectivity (stage 3)	1858 1859 1860 1861 1862 1863

## Ethics approval and consent to participate

Not applicable

## Consent for publication

Not applicable

## Data availability

Datasets of synthesized ON-center mRGCMosaics generated during the current study are available at:

<https://github.com/isetbio/isetbio/tree/main/isettools/ganglioncells/data/prebakedRGCMosaics/ONmRGCMosaics>

## Materials availability

Not applicable

## Code availability

The code used to generate the data, and various tutorials on how to use the software are available at:

1887 <https://github.com/isetbio/isetbio/tree/main>  
1888  
1889 An introduction to using the software is available at:  
1890 [https://github.com/isetbio/isetbio/wiki/Retinal-ganglion-cell-\(RGC\)-mosaics](https://github.com/isetbio/isetbio/wiki/Retinal-ganglion-cell-(RGC)-mosaics)  
1891  
1892  
1893 **Author contribution**  
1894  
1895 NPC: conceptualization, mosaic synthesis & optimization algorithms, data curation,  
1896 model validation, visualization, coding, writing of original manuscript  
1897 DHB: conceptualization, coding, reviewing and editing of manuscript  
1898 BW: conceptualization, coding, reviewing and editing of manuscript  
1899  
1900  
1901  
1902  
1903  
1904  
1905  
1906  
1907  
1908  
1909  
1910  
1911  
1912  
1913  
1914  
1915  
1916  
1917  
1918  
1919  
1920  
1921  
1922  
1923  
1924  
1925  
1926  
1927  
1928  
1929  
1930  
1931  
1932

## Appendix A Deriving cone weights to the mRGC RF centers

### A.1 Local topology-based convergent connections (stage 2A)

During the first sub-stage of cone-to-mRGC RF center connectivity, cones are connected to single mRGC RF centers based on the local topology of their respective lattices. Starting with the cell whose RF center is at most central location of the mRGC lattice, we connect  $n_{pool}(\epsilon)$  number of L- and M-cones to it, where:

$$n_{pool}(\epsilon) = \lfloor \frac{D_{cones}(\epsilon)}{D_{mRGCRF}(\epsilon)} \rfloor \quad (\text{A1})$$

with  $D_{cones}(\epsilon)$  and  $D_{mRGCRF}(\epsilon)$  being the local spatial densities of the cone mosaic and of the mRGC RF centers, respectively, at the eccentricity,  $\epsilon$ , of the target mRGC. We draw from the nearest cones that have not yet been connected and whose distance to the mRGC RF center does not exceed a fraction of the local mRGC RF center spacing. This fraction is a parameter of the model and for the work presented here was set to 0.6.

Continuing with these assignments of cones to mRGC RF centers, we move outward to more peripheral locations in the mRGC mosaic, exclusively connecting cones to mRGC RF centers. Any L- and M-cones that remain unconnected at the end of this sub-stage get connected to their nearest mRGC RF center, so that all cones are connected to one mRGC RF center.

This sub-stage can result in local inhomogeneities in both the number of cones and the type of cones pooled within neighboring mRGC RF centers. These inhomogeneities are smoothed out at stage 2B.

### A.2 Optimizing cone connections to mRGC RF centers (stage 2B)

In the second sub-stage of the cone to mRGC RF center connectivity, convergent connections from multiple cones to single mRGC RF centers are optimized according to a desired balance between spatial homogeneity and spectral purity. This is achieved by reassigning cones between nearby mRGC RF centers, which itself occurs in two steps.

In the first step, we allow cone reassessments to a target mRGC from neighboring mRGCS that have a higher input cone numerosity in their RF centers. In the second step, we allow cone swaps between a target mRGC and its neighbors, independently of their input cone numerosities.

The heuristics followed in the first step are as follows. We begin by targeting mRGCS with a single input cone and continue to target mRGCS with progressively higher input cone numerosity. Within each set of targeted input cone numerosity, mRGCS are sorted based on ascending retinal eccentricity. For each targeted mRGC we determine up to 6 neighboring mRGCS which have input numerosity that exceeds that of the target mRGC by at least 2 cones.

1979 Cone reassessments from the candidate donor mRGCs to the target mRGC are  
 1980 executed in multiple passes. Starting with the neighboring mRGC of the highest input  
 1981 numerosity, we determine the best transfer of a single cone. If there are no eligible  
 1982 donor nearby mRGCs, we move to the next targeted mRGC. If there is a single candi-  
 1983 date, we accept it and execute the cone transfer. If there are more than one candidates,  
 1984 for each candidate donor mRGC we compute a cost function,  $C$ , for reassigning each of  
 1985 its cones to the target mRGC, and pick the transfer that minimizes  $C$  across all cones  
 1986 and all candidate donor mRGCs. The cost function is described in more detail below.

1987 Once the optimal cone transfers for each mRGC of the targeted input cone  
 1988 numerosity are executed, we move to the next pass, examining possible transfers from  
 1989 neighboring mRGCs of lower input cone numerosity than before, but still higher than  
 1990 the input cone numerosity of the targeted mRGCs. Once all passes are executed, this  
 1991 process is repeated, now targeting mRGCs with increasing input cone numerosity,  
 1992 until all input cone numerosities have been targeted.

1993 In the second step, we only allow for cone swaps between an mRGC RF center and  
 1994 one of its neighbors. For each mRGC of the targeted input cone numerosity, we deter-  
 1995 mine its 6 closest neighbors, but now without regard to their input cone numerosity.  
 1996 For each of these neighboring mRGCs, we evaluate the cost function,  $C$ , for all pos-  
 1997 sible combinations of cones from the target mRGC and cones from the neighboring  
 1998 mRGC and pick the combination that minimizes  $C$ . The selected cone swap is exe-  
 1999 cuted only if the post-swap value of  $C$  is lower than its pre-swap value. Multiple passes  
 2000 through the entire mRGC mosaic are executed, with each pass targeting mRGCs with  
 2001 progressively higher input cone numerosity.

2002 The cost function,  $C$ , employed to determine the optimal transfer/swap is based on  
 2003 the position and types of the cones pooled by the target mRGC,  $t$ , and the examined  
 2004 neighboring mRGC,  $t_i$ . For each examined pair of mRGCs,  $(t, t_i)$ ,  $C^{(t, t_i)}$  is defined as:

$$2005 \quad C^{(t, t_i)} = \phi \cdot C_{\chi}^{(t, t_i)} + (1 - \phi) \cdot C_{\lambda}^{(t, t_i)} \quad (\text{A2})$$

2006 where  $C_{\chi}^{(t, t_i)}$  quantifies the degree of spatial incompactness,  $C_{\lambda}^{(t, t_i)}$  quantifies the degree  
 2007 of spectral impurity. The  $\phi$  parameter controls the desired trade-off between these  
 2008 two RF center attributes. When  $\phi = 1$ , cone reassessments/swaps are selected so as  
 2009 to minimize the degree of spatial incompactness, when  $\phi = 0$ , cone reassessments are  
 2010 chosen so as to minimize the degree of spectral impurity, and for intermediate values  
 2011 of  $\phi$ , cone reassessments are chosen so as to minimize a weighted sum of the two.

2012 The degree of spatial incompactness,  $C_{\chi}^{(t, t_i)}$ , in Eq. A2 is defined as:

$$2013 \quad C_{\chi}^{(t, t_i)} = C_{\chi_N}^{(t, t_i)} + C_{\chi_o}^{(t, t_i)} \quad (\text{A3})$$

2014 The  $C_{\chi_N}^{(t, t_i)}$  term quantifies the differential input cone numerosity between the  
 2015 examined pair of mRGCs, and is defined as:

$$2016 \quad C_{\chi_N}^{(t, t_i)} = |(N_L^t + N_M^t) - (N_L^{t_i} + N_M^{t_i})| \quad (\text{A4})$$

2017

2018

2019

2020

2021

2022

2023

2024

with  $N_L^t$  and  $N_M^t$  are the numbers of L– and M–cones pooled by the RF center of mRGC  $t$ , respectively. The  $C_{\chi_o}^{(t,t_i)}$  term is a measure of the spatial overlap of the two sets of cones pooled by the two mRGCs, and is defined as the inverse of the distance between the centroids,  $(P^t, P^{t_i})$ , of the sets of pooled cones normalized by the sum of their respective spatial standard deviations,  $(\sigma^t, \sigma^{t_i})$ :

$$C_{\chi_o}^{(t,t_i)} = 1 / \left( \frac{\|P^t - P^{t_i}\|}{\sigma^t + \sigma^{t_i}} \right) \quad (\text{A5})$$

A low value of  $C_{\chi_o}^{(t,t_i)}$  indicates low overlap between the sets of cones pooled by the examined pair of mRGCs and conversely, a high value indicates a large overlap.

The degree of spectral impurity,  $C_\lambda^{t,t_i}$ , in Eq. A2, is defined as the sum of spectral impurities of the RF centers of the pair of analyzed mRGCs:

$$C_\lambda^{t,t_i} = C_\lambda^t + C_\lambda^{t_i} \quad (\text{A6})$$

with  $C_\lambda^t$ , quantifying the degree of non-specificity, with regard to the type of cone, in the pooling within the RF center of an mRGC, defined as:

$$C_\lambda^t = \frac{\min([N_L^t, N_M^t])}{N_L^t + N_M^t} \quad (\text{A7})$$

Values of  $C_\lambda^t$  near zero indicate a low amount of mixture of L– and M–cones, and therefore a RF with a high degree of spectral purity, and conversely, values of  $C_\lambda^t$ , near 0.5, indicate an equal mixture of L– and M–cones, and therefore a RF center with a low degree of spectral purity.

### A.3 Divergent cone connections to multiple mRGC RF centers (stage 2C)

In the final sub-stage of establishing the RF center connectivity, the exclusivity of connections is relaxed, and cone connections are allowed to diverge to more than one mRGC RF center. This divergence is guided by *in-vitro* measurements of mRGC RF center overlap in the macaque [39].

According to these observations, neighboring mRGC RF centers abut at approximately one standard deviation of their Gaussian RF profile. One caveat of using these *in-vitro* measurements to establish cone divergence in the model, is that these measurements are only available in the far periphery (30–40 degrees), with no data available for more central locations. Anatomical studies suggest, however, that, in the central retina, there must be little to no divergence of cone signals to mRGCs RF centers, so we chose to implement an eccentricity-varying divergence in our model to bridge this gap.

To achieve this, we begin by fitting an ellipsoid to the spatial pooling map of cones that are exclusively connected to the RF center of an mRGC, and extract the rotation,  $\alpha$ , and the major/minor radii,  $\sigma_x, \sigma_y$  of the fitted ellipsoid. Next, a supra-Gaussian

2025  
2026  
2027  
2028  
2029  
2030  
2031  
2032  
2033  
2034  
2035  
2036  
2037  
2038  
2039  
2040  
2041  
2042  
2043  
2044  
2045  
2046  
2047  
2048  
2049  
2050  
2051  
2052  
2053  
2054  
2055  
2056  
2057  
2058  
2059  
2060  
2061  
2062  
2063  
2064  
2065  
2066  
2067  
2068  
2069  
2070

2071 ellipsoid function,  $G(x, y, n)$ , defined as:

2072

$$2073 \quad G(x, y, n) = \exp \left[ -0.5 \times \left( \sqrt{(y'^2 + y'^2)} \right)^n \right] \quad (A8)$$

2075

2076 with:

$$2077 \quad [x' \ y'] = [x \ y] \cdot \begin{bmatrix} \cos(\alpha) & -\sin(\alpha) \\ \sin(\alpha) & \cos(\alpha) \end{bmatrix} \cdot \begin{bmatrix} 1/\sigma_x & 0 \\ 0 & 1/\sigma_y \end{bmatrix} \quad (A9)$$

2079 is computed by scaling the values of  $\sigma_x, \sigma_y$  by a common factor, so that the value of  
2080  $G(x, y, n)$ , evaluated at the most remote exclusively-connected cone(s) is  $k \times e^{-1/2}$ .

2081 The value of  $k$  is determined empirically so that RF maps of nearby mRGCs computed  
2082 under diffraction-limited optics abut when their sensitivities drop to  $e^{-1/2}$  (per [39]).

2083 By varying the exponent of the supra-Gaussian,  $n$ , we model varying degrees of  
2084 cone divergence. When  $n = 10$ , we obtain a flat-top Gaussian with very sharp fall-offs,  
2085 modeling minimal cone divergence. When  $n = 2$ , we get a standard Gaussian modeling  
2086 cone divergence that is consistent with the *in-vitro* measurements of RF center overlap  
2087 at peripheral locations.

2088 By allowing  $n$  to vary with eccentricity using a sigmoidal function we obtain a  
2089 gradual transition in cone divergence with eccentricity. The slope and mid-point of the  
2090 sigmoidal variation of  $n$  are currently chosen arbitrarily, with the only restrictions that  
2091 above  $15^\circ$ ,  $n$  is stable at 2.0, and below  $7^\circ$ ,  $n$  is stable at 10.0. The weights of divergent  
2092 cone-mRGC RF center connections are computed by evaluating the supra-Gaussian  
2093 ellipsoid at the positions of all cones in the vicinity of the examined mRGC.

2094

## 2095 **Appendix B Deriving cone weights to the mRGC 2096 RF surrounds**

### 2098 **B.1 Choosing physiology-based constraints for deriving 2099 surround cone weights in stage 3B**

2101 The optimization of the parameters of the surround cone pooling functions at each  
2102 iteration is driven by the residual between the visual STF that is computed based on  
2103 the surround pooling weights at the previous iteration and the Difference of Gaussians  
2104 model fit to it,  $\text{DoG}(\omega)$ , which is given by:

2105

$$2106 \quad \text{DoG}(\omega) = K_c \cdot R_c^2 \cdot \exp[-\pi \cdot R_c \cdot \omega]^2 - K_s \cdot R_s^2 \cdot \exp[-\pi \cdot R_s \cdot \omega]^2 \quad (B10)$$

2107

2108 This aspect of the optimization captures the observation that the DoG model provides  
2109 a reasonable fit to the *in-vivo* measured STFs of macaque mRGCs. To ensure adher-  
2110 ence to the *in-vivo* data of Croner & Kaplan, the DoG model fit is constrained so  
2111 that the ratio of surround to center radii,  $R_s/R_c$ , and the ratio of surround to center  
2112 integrated sensitivities,  $K_s/K_c \times (R_s/R_c)^2$ , both remain within a specified tolerance  
2113 range from the corresponding macaque data.

2114

2115

2116

Specifically, for the model's  $R_s/R_c$  ratio, we enforce 2117  
2118

$$\frac{R_s^m}{R_c^m} \times (1 - \tau) \leq \frac{R_s}{R_c} \leq (1 + \tau) \times \frac{R_s^m}{R_c^m} \quad (\text{B11})$$

where  $R_c^m$  and  $R_s^m$  are the mean values of center and surround radii across the Croner & Kaplan population of macaque mRGCs at the eccentricity of the synthesized mRGC. The model's  $K_s/K_c \times (R_s/R_c)^2$  ratio is constrained in the same way.

The residual between the visual STF and the Difference of Gaussians model fit to it, drives the optimization of the surround pooling function. This function is a double exponent (following the H1 horizontal cell spatial RF in the macaque [43]):

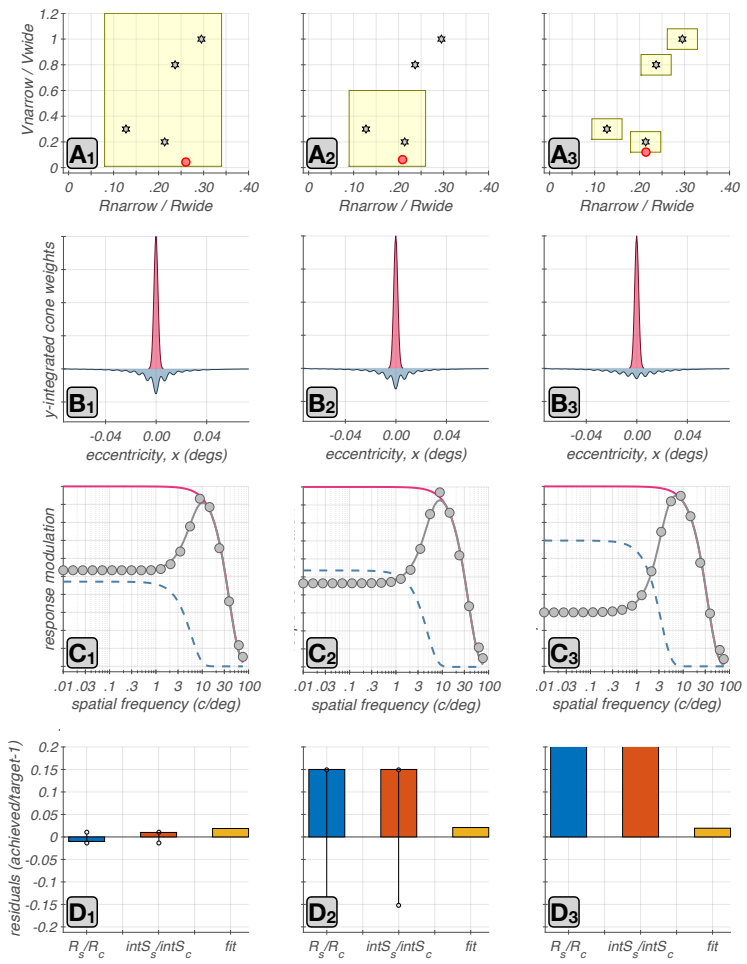
$$W_s(r) = K_{\text{wide}} \times \exp[-r/R_{\text{wide}}] + K_{\text{narrow}} \times \exp[-r/R_{\text{narrow}}] \quad (\text{B12})$$

To ensure that the surround pooling function remains consistent with the parameter values observed in macaque H1 cells [43], the optimization of  $W_s(r)$  is also constrained so that ratio of radii,  $R_{\text{narrow}}/R_{\text{wide}}$ , and the ratio of volumes,  $V_{\text{narrow}}/V_{\text{wide}} = K_{\text{narrow}}/K_{\text{wide}} \times (R_{\text{narrow}}/R_{\text{wide}})^2$ , of the two exponentials both remain within a specified tolerance range of the macaque data.

In the present work, the tolerance range for  $R_{\text{narrow}}/R_{\text{wide}}$  was set to  $[0.07, 0.35]$  for all mosaics, whereas the tolerance range for  $V_{\text{narrow}}/V_{\text{wide}}$  was set to  $[0.01, 0.6]$  for mosaics at eccentricities  $\leq 15^\circ$ , to  $[0.3, 0.9]$  for eccentricities in  $15^\circ \dots 25^\circ$ , and to  $[0.6, 1.3]$ , for eccentricities  $\geq 25^\circ$ .

The joint manipulation of the tolerance values applied to the parameters of the DoG model fit to the vSTF, and to the parameters of the double exponential surround pooling model,  $W_s(r)$ , allows for different options for deriving spatial pooling functions in synthetic mRGC surrounds.

One option is to set very strict tolerances on the parameters of DoG model fit while allowing for a large tolerance in the parameters of  $W_s(r)$ . Results of this choice are depicted in the left-most column of Figure B1. A second option would be to allow medium tolerance levels in both the DoG model fit and the  $W_s(r)$ . Results of this choice are depicted in the middle column of Figure B1. A third option would be to enforce strict tolerances in  $W_s(r)$ , for example matching parameters of individual H1 horizontal cells, while allowing for a loose tolerance in the DoG model fit. Results of this choice are depicted in the right column of Figure B1. In the present work, we chose the second option.



2163  
2164  
2165  
2166  
2167  
2168  
2169  
2170  
2171  
2172  
2173  
2174  
2175  
2176  
2177  
2178  
2179  
2180  
2181  
2182  
2183  
2184  
2185  
2186  
2187  
2188  
2189  
2190  
2191  
2192  
2193  
2194 Fig. B1 **Effect of constraints on surround cone pooling.** Results from three options for constraining the surround optimization. Left column: tight tolerance in the parameters of the DoG model fit to the vSTF and loose tolerance in the parameters of the double exponential surround pooling model,  $W_s(r)$ . Middle column: medium tolerance in both sets of parameters. Right column: loose tolerance in the DoG parameters and tight tolerance in the  $W_s(r)$  parameters. **A1-A3:** The yellow rectangles indicate the tolerance range in the joint space of the two surround cone pooling related parameters,  $V_{\text{narrow}}/V_{\text{wide}}$  and  $R_{\text{narrow}}/R_{\text{wide}}$ . Stars depict the corresponding parameter values in four macaque H1 horizontal cells from the study of Packer & Dacey. The red disk depicts the achieved parameter values under each strategy for an example foveal synthetic mRGC. **B1-B3:** Line weighting functions of the retinal space-referred center and surround cone pooling weights under the three examined strategies. **C1-C3:** The vSTF computed under the three strategies (gray disks) and corresponding DOG model fits (gray lines). The red and blue lines depict the center and surround components of the fitted DOG model. **D1-D3:** Blue and orange bars depict the residuals for the ratios of visual space-referred  $R_s/R_c$  and  $K_s/K_c \times (R_s/R_c)^2$  ratios. Black circles connected by a black line depict the enforced tolerance range in these ratios. The enforced tolerance value in D3 was  $\tau = 0.5$ , and is not visualized. The orange bars depict the  $\|v\text{STF}(\omega) - \text{DOG}(\omega)\|$  residual.

2207  
2208

<b>References</b>	2209
[1] Wandell, B.A., Brainard, D.H., Cottaris, N.P.: Visual encoding: Principles and software. <i>Prog Brain Res</i> <b>273</b> (1), 199–229 (2022) <a href="https://doi.org/10.1016/bs.pbr.2022.04.006">https://doi.org/10.1016/bs.pbr.2022.04.006</a>	2210
[2] Cottaris, N.P., Jiang, H., Ding, X., Wandell, B.A., Brainard, D.H.: A computational-observer model of spatial contrast sensitivity: Effects of wave-front-based optics, cone-mosaic structure, and inference engine. <i>J Vis</i> <b>19</b> (4), 8 (2019) <a href="https://doi.org/10.1167/19.4.8">https://doi.org/10.1167/19.4.8</a>	2211
[3] Cottaris, N.P., Wandell, B.A., Rieke, F., Brainard, D.H.: A computational observer model of spatial contrast sensitivity: Effects of photocurrent encoding, fixational eye movements, and inference engine. <i>J Vis</i> <b>20</b> (7), 17 (2020) <a href="https://doi.org/10.1167/jov.20.7.17">https://doi.org/10.1167/jov.20.7.17</a>	2212
[4] Lian, T., MacKenzie, K.J., Brainard, D.H., Cottaris, N.P., Wandell, B.A.: Ray tracing 3d spectral scenes through human optics models. <i>J Vis</i> <b>19</b> (12), 23 (2019) <a href="https://doi.org/10.1167/19.12.23">https://doi.org/10.1167/19.12.23</a>	2213
[5] Nankivil, D., Cottaris, N.P., Brainard, D.H.: Theoretical impact of chromatic aberration correction on visual acuity. <i>Biomed Opt Express</i> <b>15</b> (5), 3265–3284 (2024) <a href="https://doi.org/10.1364/BOE.516049">https://doi.org/10.1364/BOE.516049</a>	2214
[6] Zhang, L.Q., Cottaris, N.P., Brainard, D.H.: An image reconstruction framework for characterizing initial visual encoding. <i>Elife</i> <b>11</b> (2022) <a href="https://doi.org/10.7554/elife.71132">https://doi.org/10.7554/elife.71132</a>	2215
[7] Kupers, E.R., Carrasco, M., Winawer, J.: Modeling visual performance differences 'around' the visual field: A computational observer approach. <i>PLoS Comput Biol</i> <b>15</b> (5), 1007063 (2019) <a href="https://doi.org/10.1371/journal.pcbi.1007063">https://doi.org/10.1371/journal.pcbi.1007063</a>	2216
[8] Singh, V., Cottaris, N.P., Heasly, B.S., Brainard, D.H., Burge, J.: Computational luminance constancy from naturalistic images. <i>J Vis</i> <b>18</b> (13), 19 (2018) <a href="https://doi.org/10.1167/18.13.19">https://doi.org/10.1167/18.13.19</a>	2217
[9] Ding, X., Radonjic, A., Cottaris, N.P., Jiang, H., Wandell, B.A., Brainard, D.H.: Computational-observer analysis of illumination discrimination. <i>J Vis</i> <b>19</b> (7), 11 (2019)	2218
[10] Godat, T., Cottaris, N.P., Patterson, S., Kohout, K., Parkins, K., Yang, Q., Strazzeri, J.M., McGregor, J.E., Brainard, D.H., Merigan, W.H., Williams, D.R.: In vivo chromatic and spatial tuning of foveolar retinal ganglion cells in macaca fascicularis. <i>PLoS One</i> <b>17</b> (11), 0278261 (2022) <a href="https://doi.org/10.1371/journal.pone.0278261">https://doi.org/10.1371/journal.pone.0278261</a>	2219
[11] Osterberg, G., Andersen, H.: Topography of the Layer of Rods and Cones in	2220
	2221
	2222
	2223
	2224
	2225
	2226
	2227
	2228
	2229
	2230
	2231
	2232
	2233
	2234
	2235
	2236
	2237
	2238
	2239
	2240
	2241
	2242
	2243
	2244
	2245
	2246
	2247
	2248
	2249
	2250
	2251
	2252
	2253
	2254

- 2255       the Human Retina / by G. Østerberg. A. Busck, Copenhagen (1935). Includes  
 2256       bibliographical references (pages 94-96).
- 2257
- 2258 [12] Polyak, S.L.: The Retina; the Anatomy and the Histology of the Retina in Man,  
 2259       Ape, and Monkey, Including the Consideration of Visual Functions, the History  
 2260       of Physiological Optics, and the Histological Laboratory Technique, p. 607. The  
 2261       University of Chicago press, Chicago, Ill., (1941)
- 2262
- 2263 [13] Dacey, D.M.: The mosaic of midget ganglion cells in the human retina. *J Neurosci*  
 2264       **13**(12), 5334–55 (1993) <https://doi.org/10.1523/JNEUROSCI.13-12-05334.1993>
- 2265 [14] Patterson, S.S., Neitz, M., Neitz, J.: Reconciling color vision models with midget  
 2266       ganglion cell receptive fields. *Front Neurosci* **13**, 865 (2019) <https://doi.org/10.3389/fnins.2019.00865>
- 2267
- 2268 [15] Field, G.D., Gauthier, J.L., Sher, A., Greschner, M., Machado, T.A., Jepson,  
 2269       L.H., Shlens, J., Gunning, D.E., Mathieson, K., Dabrowski, W., Paninski, L.,  
 2270       Litke, A.M., Chichilnisky, E.J.: Functional connectivity in the retina at the res-  
 2271       olution of photoreceptors. *Nature* **467**(7316), 673–7 (2010) <https://doi.org/10.1038/nature09424>
- 2272
- 2273 [16] Wool, L.E., Crook, J.D., Troy, J.B., Packer, O.S., Zaidi, Q., Dacey, D.M.: Non-  
 2274       selective wiring accounts for red-green opponency in midget ganglion cells of  
 2275       the primate retina. *J Neurosci* **38**(6), 1520–1540 (2018) <https://doi.org/10.1523/JNEUROSCI.1688-17.2017>
- 2276
- 2277 [17] Croner, L.J., Kaplan, E.: Receptive fields of p and m ganglion cells across  
 2278       the primate retina. *Vision Res* **35**(1), 7–24 (1995) [https://doi.org/10.1016/0042-6989\(94\)e0066-t](https://doi.org/10.1016/0042-6989(94)e0066-t)
- 2279
- 2280 [18] Lee, B.B., Shapley, R.M., Hawken, M.J., Sun, H.: Spatial distributions of cone  
 2281       inputs to cells of the parvocellular pathway investigated with cone-isolating  
 2282       gratings. *J Opt Soc Am A Opt Image Sci Vis* **29**(2), 223–32 (2012) <https://doi.org/10.1364/JOSAA.29.00A223>
- 2283
- 2284 [19] Reid, R.C., Shapley, R.M.: Spatial structure of cone inputs to receptive fields in  
 2285       primate lateral geniculate nucleus. *Nature* **356**(6371), 716–8 (1992) <https://doi.org/10.1038/356716a0>
- 2286
- 2287 [20] Chen, Q., Ingram, N.T., Baudin, J., Angueyra, J.M., Sinha, R., Rieke, F.:  
 2288       Predictably manipulating photoreceptor light responses to reveal their role  
 2289       in downstream visual responses. *eLife* **13** (2024) <https://doi.org/10.7554/eLife.93795>
- 2290
- 2291 [21] Freeman, J., Field, G.D., Li, P.H., Greschner, M., Gunning, D.E., Mathieson, K.,  
 2292       Sher, A., Litke, A.M., Paninski, L., Simoncelli, E.P., Chichilnisky, E.J.: Mapping  
 2293       nonlinear receptive field structure in primate retina at single cone resolution. *eLife*  
 2294       **13** (2024) <https://doi.org/10.7554/eLife.93795>
- 2295
- 2296
- 2297 [22] Freeman, J., Field, G.D., Li, P.H., Greschner, M., Gunning, D.E., Mathieson, K.,  
 2298       Sher, A., Litke, A.M., Paninski, L., Simoncelli, E.P., Chichilnisky, E.J.: Mapping  
 2299       nonlinear receptive field structure in primate retina at single cone resolution. *eLife*  
 2300       **13** (2024) <https://doi.org/10.7554/eLife.93795>

- 4 (2015) <https://doi.org/10.7554/eLife.05241> 2301  
 2302
- [22] Hong, A., Rieke, F.: On-off asymmetries of nonlinear spatial integration impact the encoding of natural stimuli in primate retina. *Investigative Ophthalmology & Visual Science* **65**(7), 4346–4346 (2024) 2303  
 2304  
 2305  
 2306  
 2307  
 2308  
 2309
- [23] Raghavan, R.T., Kelly, J.G., Hasse, J.M., Levy, P.G., Hawken, M.J., Movshon, J.A.: Contrast and luminance gain control in the macaque's lateral geniculate nucleus. *eNeuro* **10**(3) (2023) <https://doi.org/10.1523/ENEURO.0515-22.2023> 2310  
 2311  
 2312  
 2313
- [24] Turner, M.H., Rieke, F.: Synaptic rectification controls nonlinear spatial integration of natural visual inputs. *Neuron* **90**(6), 1257–1271 (2016) <https://doi.org/10.1016/j.neuron.2016.05.006> 2314  
 2315  
 2316  
 2317
- [25] Benardete, E.A., Kaplan, E.: The receptive field of the primate p retinal ganglion cell, i: Linear dynamics. *Vis Neurosci* **14**(1), 169–85 (1997) <https://doi.org/10.1017/s0952523800008853> 2318  
 2319  
 2320  
 2321
- [26] Croner, L.J., Purpura, K., Kaplan, E.: Response variability in retinal ganglion cells of primates. *Proc Natl Acad Sci U S A* **90**(17), 8128–30 (1993) <https://doi.org/10.1073/pnas.90.17.8128> 2322  
 2323  
 2324  
 2325
- [27] Kling, A., Cooler, S., Manookin, M.B., Rhoades, C., Brackbill, N., Field, G., Rieke, F., Sher, A., Litke, A., Chichilnisky, E.J.: Functional diversity in the output of the primate retina. *bioRxiv* (2024) <https://doi.org/10.1101/2024.10.31.621339> 2326  
 2327  
 2328  
 2329
- [28] Pillow, J.W., Paninski, L., Uzzell, V.J., Simoncelli, E.P., Chichilnisky, E.J.: Prediction and decoding of retinal ganglion cell responses with a probabilistic spiking model. *J Neurosci* **25**(47), 11003–13 (2005) <https://doi.org/10.1523/JNEUROSCI.3305-05.2005> 2330  
 2331  
 2332  
 2333
- [29] Wohrer, A., Kornprobst, P.: Virtual retina: a biological retina model and simulator, with contrast gain control. *J Comput Neurosci* **26**(2), 219–49 (2009) <https://doi.org/10.1007/s10827-008-0108-4> 2334  
 2335  
 2336  
 2337  
 2338
- [30] Ly, K., Italiano, M.L., Shivdasani, M.N., Tsai, D., Zhang, J.Y., Jiang, C., Lovell, N.H., Dokos, S., Guo, T.: Virtual human retina: Simulating neural signalling, degeneration, and responses to electrical stimulation. *Brain Stimul* **18**(1), 144–163 (2025) <https://doi.org/10.1016/j.brs.2025.01.013> 2339  
 2340  
 2341  
 2342
- [31] Somaratna, M.A., Freeman, A.W.: The receptive field construction of midget ganglion cells in primate retina. *J Neurophysiol* **133**(1), 268–285 (2025) <https://doi.org/10.1152/jn.00302.2024> 2343  
 2344  
 2345  
 2346

- 2347 [33] Hennig, M.H., Funke, K., Worgotter, F.: The influence of different retinal sub-  
2348 circuits on the nonlinearity of ganglion cell behavior. *J Neurosci* **22**(19), 8726–38  
2349 (2002) <https://doi.org/10.1523/JNEUROSCI.22-19-08726.2002>
- 2350
- 2351 [34] Watson, A.B.: A formula for human retinal ganglion cell receptive field density  
2352 as a function of visual field location. *J Vis* **14**(7) (2014) <https://doi.org/10.1167/14.7.15>
- 2352
- 2353
- 2354 [35] Curcio, C.A., Allen, K.A.: Topography of ganglion cells in human retina. *J Comp  
2355 Neurol* **300**(1), 5–25 (1990) <https://doi.org/10.1002/cne.903000103>
- 2356
- 2357 [36] Curcio, C.A., Sloan, K.R., Kalina, R.E., Hendrickson, A.E.: Human photoreceptor  
2358 topography. *J Comp Neurol* **292**(4), 497–523 (1990) <https://doi.org/10.1002/cne.902920402>
- 2359
- 2360
- 2361 [37] Klug, K., Herr, S., Ngo, I.T., Sterling, P., Schein, S.: Macaque retina contains an  
2362 s-cone off midget pathway. *J Neurosci* **23**(30), 9881–7 (2003) <https://doi.org/10.1523/JNEUROSCI.23-30-09881.2003>
- 2363
- 2364
- 2365 [38] Patterson, S.S., Kuchenbecker, J.A., Anderson, J.R., Bordt, A.S., Marshak, D.W.,  
2366 Neitz, M., Neitz, J.: An s-cone circuit for edge detection in the primate retina.  
2367 *Sci Rep* **9**(1), 11913 (2019) <https://doi.org/10.1038/s41598-019-48042-2>
- 2368
- 2369 [39] Gauthier, J.L., Field, G.D., Sher, A., Shlens, J., Greschner, M., Litke, A.M.,  
2370 Chichilnisky, E.J.: Uniform signal redundancy of parasol and midget ganglion  
2371 cells in primate retina. *J Neurosci* **29**(14), 4675–80 (2009) <https://doi.org/10.1523/JNEUROSCI.5294-08.2009>
- 2372
- 2373
- 2374 [40] Kling, A., Gogliettino, A.R., Shah, N.P., Wu, E.G., Brackbill, N., Sher, A., Litke,  
2375 A.M., Silva, R.A., Chichilnisky, E.J.: Functional organization of midget and para-  
2376 sol ganglion cells in the human retina (2020) <https://doi.org/10.1101/2020.08.07.240762>
- 2377
- 2378
- 2379 [41] Kolb, H., Marshak, D.: The midget pathways of the primate retina. *Doc  
2380 Ophthalmol* **106**(1), 67–81 (2003) <https://doi.org/10.1023/a:1022469002511>
- 2381
- 2382 [42] McMahon, M.J., Lankheet, M.J., Lennie, P., Williams, D.R.: Fine structure of  
2383 parvocellular receptive fields in the primate fovea revealed by laser interferometry.  
2384 *J Neurosci* **20**(5), 2043–53 (2000) <https://doi.org/10.1523/JNEUROSCI.20-05-02043.2000>
- 2385
- 2386 [43] Packer, O.S., Dacey, D.M.: Receptive field structure of h1 horizontal cells in  
2387 macaque monkey retina. *J Vis* **2**(4), 272–92 (2002) <https://doi.org/10.1167/2.4.1>
- 2388
- 2389 [44] Smith, V.C., Lee, B.B., Pokorny, J., Martin, P.R., Valberg, A.: Responses  
2390 of macaque ganglion cells to the relative phase of heterochromatically modu-  
2391 lated lights. *J Physiol* **458**, 191–221 (1992) <https://doi.org/10.1113/jphysiol.1992.2392>
- 2392

- |   |      |
|---|------|
| sp019413  | 2393 |
|   | 2394 |
| [45] Polans, J., Jaeken, B., McNabb, R.P., Artal, P., Izatt, J.A.: Wide-field optical model of the human eye with asymmetrically tilted and decentered lens that reproduces measured ocular aberrations. <i>Optica</i> <b>2</b> (2), 124–134 (2015) <a href="https://doi.org/10.1364/OPTICA.2.000124">https://doi.org/10.1364/OPTICA.2.000124</a>   | 2395 |
|   | 2396 |
|   | 2397 |
|   | 2398 |
|   | 2399 |
| [46] Gogliettino, A.R., Madugula, S.S., Grosberg, L.E., Vilkhu, R.S., Brown, J., Nguyen, H., Kling, A., Hottowy, P., Dabrowski, W., Sher, A., Litke, A.M., Chichilnisky, E.J.: High-fidelity reproduction of visual signals by electrical stimulation in the central primate retina. <i>J Neurosci</i> <b>43</b> (25), 4625–4641 (2023) <a href="https://doi.org/10.1523/JNEUROSCI.1091-22.2023">https://doi.org/10.1523/JNEUROSCI.1091-22.2023</a> | 2400 |
|   | 2401 |
|   | 2402 |
|   | 2403 |
|   | 2404 |
|   | 2405 |
| [47] Packer, O., Hendrickson, A.E., Curcio, C.A.: Photoreceptor topography of the retina in the adult pigtail macaque ( <i>macaca nemestrina</i> ). <i>J Comp Neurol</i> <b>288</b> (1), 165–83 (1989) <a href="https://doi.org/10.1002/cne.902880113">https://doi.org/10.1002/cne.902880113</a>  | 2406 |
|   | 2407 |
|   | 2408 |
| [48] Drasdo, N., Fowler, C.W.: Non-linear projection of the retinal image in a wide-angle schematic eye. <i>Br J Ophthalmol</i> <b>58</b> (8), 709–14 (1974) <a href="https://doi.org/10.1136/bjo.58.8.709">https://doi.org/10.1136/bjo.58.8.709</a>  | 2409 |
|   | 2410 |
|   | 2411 |
|   | 2412 |
| [49] Perry, V.H., Cowey, A.: The ganglion cell and cone distributions in the monkey's retina: implications for central magnification factors. <i>Vision Res</i> <b>25</b> (12), 1795–810 (1985) <a href="https://doi.org/10.1016/0042-6989(85)90004-5">https://doi.org/10.1016/0042-6989(85)90004-5</a>   | 2413 |
|   | 2414 |
|   | 2415 |
|   | 2416 |
| [50] Tuten, W.S., Cooper, R.F., Tiruveedhula, P., Dubra, A., Roorda, A., Cottaris, N.P., Brainard, D.H., Morgan, J.I.W.: Spatial summation in the human fovea: Do normal optical aberrations and fixational eye movements have an effect? <i>J Vis</i> <b>18</b> (8), 6 (2018) <a href="https://doi.org/10.1167/18.8.6">https://doi.org/10.1167/18.8.6</a>  | 2417 |
|   | 2418 |
|   | 2419 |
|   | 2420 |
|   | 2421 |
| [51] Schein, S.J.: Anatomy of macaque fovea and spatial densities of neurons in foveal representation. <i>J Comp Neurol</i> <b>269</b> (4), 479–505 (1988) <a href="https://doi.org/10.1002/cne.902690403">https://doi.org/10.1002/cne.902690403</a>  | 2422 |
|   | 2423 |
|   | 2424 |
|   | 2425 |
|   | 2426 |
|   | 2427 |
|   | 2428 |
| [52] Grunert, U., Martin, P.R.: Cell types and cell circuits in human and non-human primate retina. <i>Prog Retin Eye Res</i> , 100844 (2020) <a href="https://doi.org/10.1016/j.preteyeres.2020.100844">https://doi.org/10.1016/j.preteyeres.2020.100844</a>   | 2429 |
|   | 2430 |
|   | 2431 |
|   | 2432 |
|   | 2433 |
|   | 2434 |
|   | 2435 |
| [53] Banks, M.S., Geisler, W.S., Bennett, P.J.: The physical limits of grating visibility. <i>Vision Res</i> <b>27</b> (11), 1915–24 (1987) <a href="https://doi.org/10.1016/0042-6989(87)90057-5">https://doi.org/10.1016/0042-6989(87)90057-5</a>   | 2436 |
|   | 2437 |
|   | 2438 |

- 2439       **10**(10), 2118–33 (1993) <https://doi.org/10.1364/josaa.10.002118>
- 2440
- 2441 [56] Casile, A., Victor, J.D., Rucci, M.: Contrast sensitivity reveals an oculomotor  
2442 strategy for temporally encoding space. *Elife* **8** (2019) <https://doi.org/10.7554/elife.40924>
- 2444
- 2445 [57] Houston, A.J.H., Brainard, D.H., Smithson, H.E., Read, D.J.: Information, move-  
2446 ment and adaptation in human vision. *bioRxiv*, 2025–0905674315 (2025) <https://doi.org/10.1101/2025.09.05.674315>
- 2447
- 2448 [58] Mullen, K.T.: The contrast sensitivity of human colour vision to red-green and  
2449 blue-yellow chromatic gratings. *J Physiol* **359**, 381–400 (1985) <https://doi.org/10.1113/jphysiol.1985.sp015591>
- 2450
- 2451
- 2452 [59] Chaparro, A., Stromeier, r. C. F., Huang, E.P., Kronauer, R.E., Eskew, J. R. T.:  
2453 Colour is what the eye sees best. *Nature* **361**(6410), 348–50 (1993) <https://doi.org/10.1038/361348a0>
- 2454
- 2455
- 2456 [60] Sekiguchi, N., Williams, D.R., Brainard, D.H.: Aberration-free measurements of  
2457 the visibility of isoluminant gratings. *J Opt Soc Am A Opt Image Sci Vis* **10**(10),  
2458 2105–17 (1993) <https://doi.org/10.1364/josaa.10.002105>
- 2459
- 2460 [61] Hong, F., Cottaris, N.P., Brainard, D.H.: Limits on human contrast sensitivity  
2461 imposed by the initial visual encoding. *Journal of Vision* **24**(10), 658–658 (2024)  
2462 <https://doi.org/10.1167/jov.24.10.658>
- 2463
- 2464 [62] Cruz, Y.T., He, J., Eskew, J. Rhea T.: Using s-cone signals to detect the effects  
2465 of longitudinal chromatic aberration. *Journal of Vision* **19**(15), 6–6 (2019) <https://doi.org/10.1167/19.15.6>
- 2466
- 2467 [63] Oh, S., Hong, F., Nankivil, D., Haggerty, E.B., Stauble, R., Cottaris, N.P., Buch,  
2468 J., Aguirre, G.K., Brainard, D.H.: Variations in human optics explain idiosyn-  
2469 cratic patterns in the red-green spatial contrast sensitivity function. *Journal of  
2470 Vision* **25**(9), 2440–2440 (2025) <https://doi.org/10.1167/jov.25.9.2440>
- 2471
- 2472 [64] Hansen, T., Pracejus, L., Gegenfurtner, K.R.: Color perception in the interme-  
2473 diate periphery of the visual field. *J Vis* **9**(4), 26–112 (2009) <https://doi.org/10.1167/9.4.26>
- 2474
- 2475
- 2476 [65] Stockman, A., Brainard, D.H.: In: Bass, M., DeCusatis, C., Enoch, J., Laksh-  
2477 minarayanan, V., Li, G., Macdonald, C., Mahajan, V., Stryland, E. (eds.) *Color  
2478 vision mechanisms*, pp. 11–111104. McGraw Hill, New York (2010)
- 2479
- 2480 [66] Lennie, P., Haake, P.W., Williams, D.R.: In: Landy, M.S., Movshon, J.A. (eds.)  
2481 The design of chromatically opponent receptive fields, pp. 71–82. MIT Press,  
2482 Cambridge, Mass. (1991). TY - JOUR
- 2483
- 2484

- [67] Mullen, K.T., Kingdom, F.A.: Losses in peripheral colour sensitivity predicted from "hit and miss" post-receptoral cone connections. *Vision Res* **36**(13), 1995–2000 (1996) [https://doi.org/10.1016/0042-6989\(95\)00261-8](https://doi.org/10.1016/0042-6989(95)00261-8) 2485  
2486  
2487  
2488  
2489
- [68] Wandell, B.A.: Foundations of Vision. Sinauer, Sunderland, MA (1995) 2490  
2491  
2492  
2493  
2494
- [69] Kim, Y.J., Packer, O., Pollreisz, A., Martin, P.R., Grunert, U., Dacey, D.M.: Comparative connectomics reveals noncanonical wiring for color vision in human foveal retina. *Proc Natl Acad Sci U S A* **120**(18), 2300545120 (2023) <https://doi.org/10.1073/pnas.2300545120> 2495  
2496  
2497  
2498  
2499
- [70] Sun, H., Ruttiger, L., Lee, B.B.: The spatiotemporal precision of ganglion cell signals: a comparison of physiological and psychophysical performance with moving gratings. *Vision Res* **44**(1), 19–33 (2004) <https://doi.org/10.1016/j.visres.2003.08.017> 2500  
2501  
2502  
2503
- [71] Angueyra, J.M., Rieke, F.: Origin and effect of phototransduction noise in primate cone photoreceptors. *Nat Neurosci* **16**(11), 1692–700 (2013) <https://doi.org/10.1038/nn.3534> 2504  
2505  
2506  
2507  
2508  
2509  
2510  
2511  
2512  
2513  
2514  
2515  
2516  
2517  
2518  
2519  
2520  
2521  
2522  
2523  
2524  
2525  
2526  
2527  
2528  
2529  
2530
- [72] Roy, S., Jun, N.Y., Davis, E.L., Pearson, J., Field, G.D.: Inter-mosaic coordination of retinal receptive fields. *Nature* **592**(7854), 409–413 (2021) <https://doi.org/10.1038/s41586-021-03317-5>